Supporting information to: Quantitative measurement of the optical cross-sections of single nano-objects by correlative transmission and scattering micro-spectroscopy

Attilio Zilli,[1,*] Wolfgang Langbein,[2] and Paola Borri[1]

[1] *Cardiff University School of Biosciences, Museum Avenue, Cardiff CF10 3AX, UK*

[2] *Cardiff University School of Physics and Astronomy, The Parade, Cardiff CF24 3AA, UK*

(Dated: 20th July 2019)

(37 pages, 9 figures, 1 table)

S.I. EXPERIMENTAL SET-UP AND PROTOCOL

Our experimental set-up is based on a commercial inverted microscope (Nikon, Eclipse Ti-U), with some customization. Incoherent broadband illumination for micro-spectroscopy is provided by a tungsten-halogen lamp (Nikon, 17005M28). Incoherent illumination with a narrow spectral range for widefield imaging is provided by a multiple light-emitting diode (LED) source (Thorlabs, LED4D067, 405 nm, 455 nm, 530 nm, 660 nm LEDs) coupled to the microscope using a liquid light guide (Thorlabs LLG0538-6). The average emission wavelength $\langle\lambda\rangle$ of the LEDs reported in Fig. 5 of the paper depends slightly on the intensity and has been characterized in house. The illumination is focused on the sample by a 1.34 numerical aperture (NA) oil-immersion condenser lens (Nikon MEL41410, T-C-HNAO). An engineered diffuser (Thorlabs, ED1-C20) inserted in the illumination path in front of the field iris yields a flat angular scattering pattern up to a $\pm 10°$ divergence, and provides thereby a quasi-homogeneous illumination intensity in the back focal plane (BFP) of the condenser as assumed by our analytical model of the illumination, see the characterization in Sec. S.VI. A wire-grid polarizing film (MeCan, WGF$^{\text{TM}}$) can be inserted in front of the condenser and rotated to produce a linear polarization of adjustable orientation in the BFP of the condenser. The sample holder is mounted on an xyz piezoelectric stage (Mad City Labs Nano-LP200), which is used for fine positioning and focusing of the nano-object (NanO). Light is collected by a 40x, 0.95 NA dry objective (Nikon MRD00405, CFI plan apochromat λ series).

The angular range of illumination is defined by suitable light stops placed in the BFP of the condenser as depicted in Fig. 1 of the paper. In order to achieve darkfield (DF) illumination of $\underline{\mathrm{NA}}_{\mathrm{i}}^{\mathrm{DF}} = 1.1$ we cut an anodized aluminum disc of diameter $2f_{\mathrm{c}}\underline{\mathrm{NA}}_{\mathrm{i}}^{\mathrm{DF}} = 23.1\,\mathrm{mm}$, calculated based on the condenser focal length $f_{\mathrm{c}} = 10.5\,\mathrm{mm}$. The disc is mounted on a slider, to permit rapid switching between brightfield (BF) and DF modalities with no need to move the condenser. The aperture diaphragm of the condenser is closed down to $\overline{\mathrm{NA}}_{\mathrm{i}}^{\mathrm{BF}} = 0.95$ in BF, matching the objective NA; and to $\overline{\mathrm{NA}}_{\mathrm{i}}^{\mathrm{DF}}$ between 1.2 and 1.3 in DF, excluding the highest NA range of the condenser to reduce deviations from the aplanatic behavior.

Micro-spectroscopy is performed by optically coupling the microscope output to an imaging spectrometer (Horiba Jobin-Yvon, iHR550) equipped with a ruled plane diffraction grating (Horiba, 510 48) of 78 mm side length and 100 lines/mm blazed at 450 nm. The spectrometer output is recorded by a Peltier-cooled back-illuminated charge-coupled device (CCD) sensor (Andor, Newton DU-971N). A magnification of 79 ± 2 from the sample to the sensor was measured shifting the sample by a known amount via the nanometric stage. Since the cross-sections are proportional to the inverse square of the magnification via A in Eq. (7) of the paper, determining its precise value is important for quantitative analysis. The spectrometer is operated first in imaging mode (i. e. with the grating oriented at the zero order of diffraction acting as a mirror) to individuate the NanO and center it with respect to

* attilio.zilli@polimi.it; Present address: Department of Physics, Politecnico di Milano – Piazza Leonardo da Vinci 32, 20133 Milano, Italy

the input slit of the spectrometer. The four detected signals appearing in Eq. (7) of the paper are then acquired in spectroscopic mode (i. e. with the grating oriented at the first order of diffraction). A square detection region $A_{\mathrm{NO}} = 1.0\,\mu\mathrm{m}^2$ is defined on the scaled sample image, delimited by the input slit and the detected size along the slit on the CCD: This is chosen large enough to accommodate the diffraction-limited image of the NanO, leaving additionally some room for spatial drift over the measurement time ($\sim 10\,\mathrm{s}$). A_{bg} corresponds to another similar-sized region of the sensor, displaced along the input slit, so that $S_{\mathrm{NO}}^{\mathrm{DF}}$ and $S_{\mathrm{bg}}^{\mathrm{DF}}$ are acquired simultaneously. This is not problematic because DF can offer a large contrast with respect to the background. In BF, conversely, the pixel-to-pixel variations of quantum efficiency ($\sim 1\,\%$) are comparable to the difference between $S_{\mathrm{NO}}^{\mathrm{BF}}$ and $S_{\mathrm{bg}}^{\mathrm{BF}}$ for the NanOs we studied. Therefore the signals must be acquired sequentially using the same region of the sensor and shifting the sample instead, so that an empty area nearby the NanO is imaged. In addition, adjacent regions of the sensor are used in BF to monitor the illumination intensity – which fluctuates $\sim 1\,\%/\mathrm{min}$ – and scale the $S_{\mathrm{bg}}^{\mathrm{BF}}$ accordingly.

Widefield imaging is performed using a monochrome low noise scientific complementary metal-oxide-semiconductor (sCMOS) camera (PCO Edge 5.5) attached to the Ti-U eyepiece side port. For automated image analysis we rely on the ImageJ Plug-in Extinction Suite [S1] developed within our group. We briefly discuss here the scattering measurements presented in the paper; we refer the reader to previous works [S2, S3] for a detailed description of the technique, also presenting its application to absorbing NanOs. We acquire one BF and one DF image. 2560 frames of exposure time 1 ms were averaged in BF. 4 frames of exposure time 1 s were averaged in DF. Between the acquisition of the two images the sample was laterally displaced by 2.2 µm – just above the characteristic point spread function (PSF) size $3\lambda/\mathrm{NA}$ for the longest measured wavelength – with the nanometric stage. The BF image serves as reference to create a quantitative scattering image. Extinction Suite individuates in this image all the intensity maxima, which correspond to the PSFs of individual NanOs or unresolved aggregates. The user sets by hand a tolerance level to avoid including small debris or background fluctuations in the analysis. Afterward the image is integrated over a disc (A_{NO}) of radius r_{PSF} and an annulus (A_{bg}) of inner radius r_{PSF} and outer radius approximately $\sqrt{2}r_{\mathrm{PSF}}$, both centered at each intensity maximum. The integrated values over A_{NO} and A_{bg} are the scattering signal and the local background, corresponding respectively to $S_{\mathrm{NO}}^{\mathrm{DF}}/S_{\mathrm{bg}}^{\mathrm{BF}}$ and $S_{\mathrm{bg}}^{\mathrm{DF}}/S_{\mathrm{bg}}^{\mathrm{BF}}$ appearing in Eq. (7s) of the paper.

For each exciting wavelength λ we used $r_{\mathrm{PSF}} = 3\lambda/2\mathrm{NA}_{\mathrm{obj}}$. In the ideal case of an Airy PSF, r_{PSF} corresponds approximately to the radius of the second dark ring, and A_{NO} contains 91 % of the collected power. However, for real microscopes objectives the PSF is modified by the vectorial nature of light and aberrations. We therefore measured σ_{sca} as a function of r_{PSF} on a few well-isolated scatterers and found that, with respect to large r_{PSF} values, (79, 90, 83)% of power is collected at $\lambda = (414, 530, 652)\,\mathrm{nm}$. These factors were used to correct the measured σ_{sca} of Fig. 5 of the paper.

S.II. NUMERICAL MODELING

We simulate optical scattering and absorption by an individual NanO using the commercial software COMSOL Multiphysics®, which implements the finite element method within a convenient user interface. The simulation volume is a sphere centered at the origin of radius $\lambda/[2\min(n_1, n_2)]$, enough to put the boundaries outside the reactive near-field region of the NanO. The sphere is halved into two media: Illumination comes from medium 1 (substrate) and the NanO is placed in medium 2 in contact with the interface. This arrangement reproduces the experimental set-up depicted in Fig. 1 of the paper. The sphere is surrounded by a perfectly matched layer (PML) shell of thickness $\lambda/(n_1+n_2)$, which absorbs the scattered radiation and thereby mimics an infinitely extended simulation volume. After refining the mesh so that the simulated cross-sections have converged within a few percent tolerance, our model has about 10^5 degrees of freedom and solves in approximately 15 s on a modern workstation (Intel Core i7-8700K CPU, 64 GB RAM).

We solve the electromagnetic problem in its frequency-domain formulation

$$\nabla \times \Big(\nabla \times \boldsymbol{E}\Big) - \omega^2 \varepsilon \mu \boldsymbol{E} = i\omega\mu \boldsymbol{J}. \tag{S1}$$

We adopt the so-called scattered field formalism, and decompose the total electric field into the scattered and the exciting field: $\boldsymbol{E}_{\text{tot}} = \boldsymbol{E}_{\text{sca}} + \boldsymbol{E}_{\text{exc}}$. $\boldsymbol{E}_{\text{exc}}$ is given by a plane wave incident on the n_1 to n_2 interface and the resulting transmitted and reflected waves, and is input via its analytical expression derived in Sec. S.III. Such analytical approach improves the model performance by a factor 5 to 10 with respect to the widespread practice of computing $\boldsymbol{E}_{\text{exc}}$ numerically with a preliminary solving step. Linearly polarized illumination in the BFP of the condenser is obtained as a superposition of the p and s polarized components with appropriate coefficients depending the azimuth φ_{i}. Unpolarized illumination is reproduced instead by averaging results obtained with p and s polarization, since the two components are mutually incoherent. $\boldsymbol{E}_{\text{sca}}$ is solved for by the software, and can be used to compute the power scattered P_{sca} and absorbed P_{abs} by the NanO. P_{sca} is the flux of the time-averaged Poynting vector of the scattered field across the surface Σ_{NO} of the NanO

$$P_{\text{sca}} = \frac{1}{2}\int_{\Sigma_{\text{NO}}} \text{Re}\left(\boldsymbol{E}_{\text{sca}} \times \boldsymbol{H}^*_{\text{sca}}\right) \cdot \widehat{\boldsymbol{n}}\ \text{d}\Sigma \tag{S2}$$

where $\widehat{\boldsymbol{n}}$ is the outside normal of Σ_{NO}. P_{abs} is computed by integrating the power dissipated via resistive (Joule) heating over the volume V_{NO} of the NanO

$$P_{\text{abs}} = \frac{1}{2}\int_{V_{\text{NO}}} \text{Re}\left(\boldsymbol{J}_{\text{c}} \cdot \boldsymbol{E}^*_{\text{tot}}\right)\ \text{d}V \tag{S3}$$

where $\boldsymbol{J}_{\text{c}} = \omega\,\text{Im}(\varepsilon)\boldsymbol{E}$ is the conduction current density in the metal. Eventually, σ_{sca} and σ_{abs} can be computed using their definition $\sigma \equiv P/I_{\text{i}}$ and Eq. (S.II).

Now, note that σ_{sca} and σ_{abs} depend on the incidence direction $(\theta_{\text{i}}, \varphi_{\text{i}})$ of the plane wave $\boldsymbol{E}_{\text{exc}}$, as well as on its polarization state. We reproduce the illumination provided by a high-NA condenser in experiments by averaging $\sigma(\theta_{\text{i}}, \varphi_{\text{i}})$ over the angular range of illumination

with the formulae derived in Sec. S.IV B. The weights used in the formulae originate from the analytical description of the microscope illumination reported in Sec. S.IV A, and account as well for the experimental referencing of σ to the measured intensity, that is, the incident intensity projected onto the sample plane. This approach – whereby $\boldsymbol{E}_{\mathrm{exc}}$ with different $(\theta_{\mathrm{i}}, \varphi_{\mathrm{i}})$ do not interfere – is consistent with the description of the microscope illumination as an incoherent superposition of plane waves adopted by our analytical model of scattering described in Sec. S.V below.

S.III. ELECTRIC FIELD ABOVE AND BELOW A DIELECTRIC INTERFACE

An analytical expression of the exciting electric field $\boldsymbol{E}_{\mathrm{exc}}$ is required both for simulating numerically the optical cross-sections of a NanO with the scattered field formalism discussed in Sec. S.II, and for the analytical calculation of the angular distribution of the scattered power, which will be presented in Sec. S.V B.

A. Illumination geometry and plane wave illumination

In this section $\boldsymbol{E}_{\mathrm{exc}}$ is derived for the general case discussed in this work, that is, two homogeneous dielectric media separated by an infinite planar interface. The experimental geometry and the notation adopted are presented in Fig. S1. Since in this work we treat the microscope illumination as an incoherent superposition of plane waves, we need to compute $\boldsymbol{E}_{\mathrm{exc}}$ above and below the interface for a plane wave impinging from the condenser side, i. e. medium 1. At the interface, the incident (subscript i) wavefront is split into a reflected (r) and a transmitted (t) one. The plane represented in Fig. S1a contains the wavevectors $\boldsymbol{k}$ of the three waves and is called *plane of incidence*. The directions parallel (p) and perpendicular (s) to the plane of incidence constitute the natural basis to decompose $\boldsymbol{E}$, because the p and s components do not mix upon transmission and reflection. It is convenient to introduce the notation $\widehat{\boldsymbol{p}} \equiv \widehat{\boldsymbol{E}}_{\mathrm{p}}$ and $\widehat{\boldsymbol{s}} \equiv \widehat{\boldsymbol{E}}_{\mathrm{s}}$.

Consider now the spherical unit vectors shown in Fig. S1b, whose expressions in Cartesian coordinates read

$$\widehat{\boldsymbol{r}} = \begin{bmatrix} \sin\theta\cos\varphi \\ \sin\theta\sin\varphi \\ \cos\theta \end{bmatrix}, \qquad \widehat{\boldsymbol{\theta}} = \begin{bmatrix} \cos\theta\cos\varphi \\ \cos\theta\sin\varphi \\ -\sin\theta \end{bmatrix}, \qquad \widehat{\boldsymbol{\varphi}} = \begin{bmatrix} -\sin\varphi \\ \cos\varphi \\ 0 \end{bmatrix}. \tag{S4}$$

Comparing these to the wavevectors and fields of the three waves in Fig. S1a, one finds that the two vector triads have always the same directions: $(\widehat{\boldsymbol{k}}, \widehat{\boldsymbol{p}}, \widehat{\boldsymbol{s}}) = (-\widehat{\boldsymbol{r}}, \widehat{\boldsymbol{\theta}}, \widehat{\boldsymbol{\varphi}})$. Therefore, the wavevector of the incident wave is $\boldsymbol{k}_{\mathrm{i}} = -k_{\mathrm{i}}\,\widehat{\boldsymbol{r}}(\theta_{\mathrm{i}}, \varphi_{\mathrm{i}})$, and equivalent expressions hold for the reflected ($\mathrm{i} \to \mathrm{r}$) and transmitted ($\mathrm{i} \to \mathrm{t}$) waves; the respective wavenumbers are $k_{\mathrm{i}} = k_{\mathrm{r}} = n_1 k_0$

and $k_\mathrm{t} = n_2 k_0$. As for the field orientations, one has $\widehat{\boldsymbol{p}}_\mathrm{i} = \widehat{\boldsymbol{\theta}}(\theta_\mathrm{i}, \varphi_\mathrm{i})$ and $\widehat{\boldsymbol{s}}_\mathrm{i} = \widehat{\boldsymbol{\varphi}}(\varphi_\mathrm{i})$ for the incident wave, and equivalent expressions hold for the reflected and transmitted ones.

The propagation direction $\widehat{\boldsymbol{k}}$ of these waves is thus identified by a polar angle θ and an azimuth φ. The polar angles are related through the law of specular reflection $\theta_\mathrm{r} = \pi - \theta_\mathrm{i}$ and Snell's law $n_1 \sin\theta_\mathrm{i} = n_2 \sin\theta_\mathrm{t}$. The planar character of the problem implies $\varphi_\mathrm{i} = \varphi_\mathrm{r} = \varphi_\mathrm{t}$ for the azimuths. Note that the alternative formulation $\theta_\mathrm{r} = \theta_\mathrm{i}$ and $\varphi_\mathrm{r} = \varphi_\mathrm{i} + \pi$ of the law of specular reflection — albeit more common in literature — would not allow the identification $(\widehat{\boldsymbol{k}}, \widehat{\boldsymbol{p}}, \widehat{\boldsymbol{s}}) = (-\widehat{\boldsymbol{r}}, \widehat{\boldsymbol{\theta}}, \widehat{\boldsymbol{\varphi}})$ for the reflected wave. The transmission and reflection amplitudes are

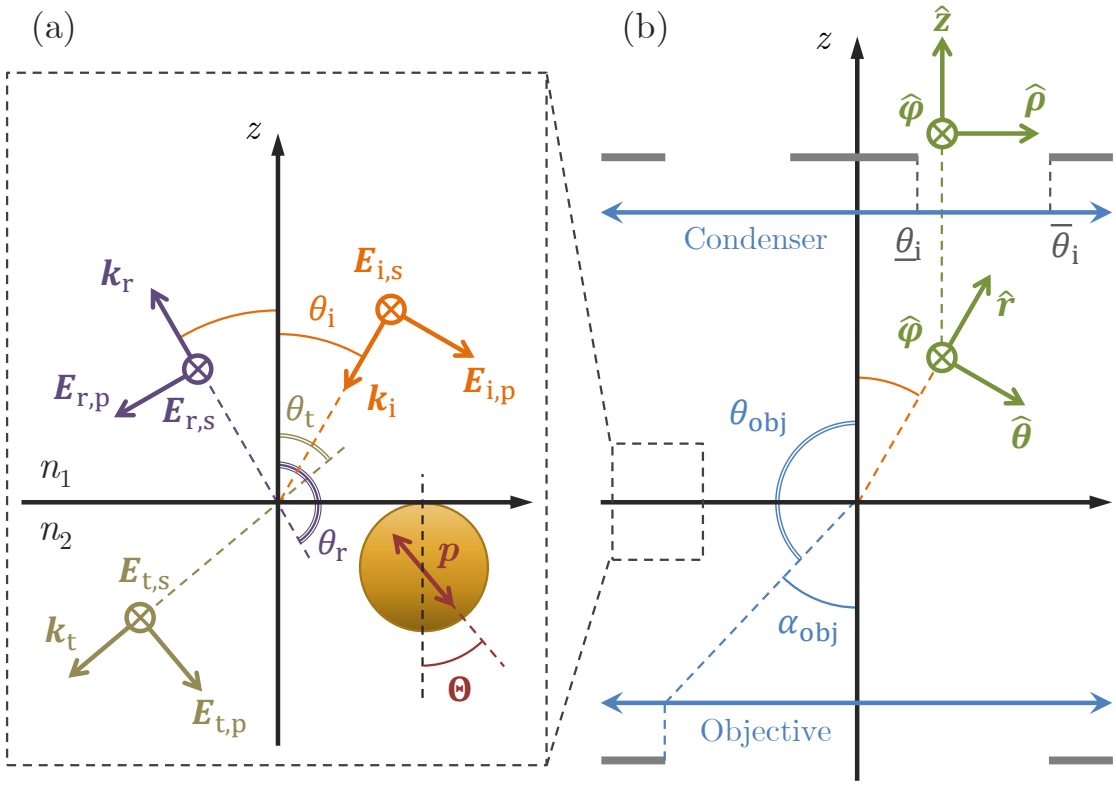

Figure S1. (a) Two homogeneous dielectric media with refractive indices n_1 and n_2 are separated by the plane $z = 0$. A plane wave $\boldsymbol{E}_\mathrm{i}$ incident on the interface splits into a reflected wave $\boldsymbol{E}_\mathrm{r}$ and a transmitted wave $\boldsymbol{E}_\mathrm{t}$. The plane of incidence $\varphi = \varphi_\mathrm{i}$ is represented, so that the p and s component of the fields are, respectively, parallel and perpendicular to the drawing plane. The field orientation depicted corresponds to $n_1 > n_2$ and $\theta_\mathrm{B} < \theta_\mathrm{i} < \theta_\mathrm{c}$, where θ_B and θ_c indicate Brewster's and critical angle, respectively. The exciting field induces an electric dipole moment $\boldsymbol{p}$ in a NanO placed near the interface, which forms an angle Θ with respect to the normal to the interface. (b) The angular ranges of illumination $\theta_\mathrm{i} \in [\underline{\theta}_\mathrm{i}, \overline{\theta}_\mathrm{i}]$ and collection $\theta \in [\theta_\mathrm{obj}, \pi]$ are determined by circular light stops placed in the back focal plane of the condenser and objective lens. Cylindrical (ρ, z, φ) and spherical (r, θ, φ) coordinates (green unit vectors) are employed respectively in the back and front spaces of the two lenses. (a) is a close-up on the interface in (b), as indicated by the dashed frames.

expressed by the *Fresnel coefficients* for p and s polarization. Under the assumptions of non-magnetic ($\mu_1 = \mu_2 = 1$), non-absorbing ($\varepsilon_{1,2} = n_{1,2}^2$) media they are

$$t_\mathrm{p} = \frac{2n_1 \cos\theta_\mathrm{i}}{n_2 \cos\theta_\mathrm{i} + n_1 \cos\theta_\mathrm{t}}, \qquad r_\mathrm{p} = \frac{n_2}{n_1} t_\mathrm{p} - 1, \tag{S5p}$$

$$t_\mathrm{s} = \frac{2n_1 \cos\theta_\mathrm{i}}{n_1 \cos\theta_\mathrm{i} + n_2 \cos\theta_\mathrm{t}}, \qquad r_\mathrm{s} = t_\mathrm{s} - 1. \tag{S5s}$$

We have now established a formalism which permits to write a compact expression of the field components

$$\boldsymbol{E}_{\mathrm{i,p}} = E_\mathrm{i}\, \widehat{\boldsymbol{p}}_\mathrm{i}\, e^{i\boldsymbol{k}_\mathrm{i}\cdot\boldsymbol{r}}, \qquad \boldsymbol{E}_{\mathrm{r,p}} = r_\mathrm{p}\, E_\mathrm{i}\, \widehat{\boldsymbol{p}}_\mathrm{r}\, e^{i\boldsymbol{k}_\mathrm{r}\cdot\boldsymbol{r}}, \qquad \boldsymbol{E}_{\mathrm{t,p}} = t_\mathrm{p}\, E_\mathrm{i}\, \widehat{\boldsymbol{p}}_\mathrm{t}\, e^{i\boldsymbol{k}_\mathrm{t}\cdot\boldsymbol{r}}, \tag{S6p}$$

$$\boldsymbol{E}_{\mathrm{i,s}} = E_\mathrm{i}\, \widehat{\boldsymbol{s}}_\mathrm{i}\, e^{i\boldsymbol{k}_\mathrm{i}\cdot\boldsymbol{r}}, \qquad \boldsymbol{E}_{\mathrm{r,s}} = r_\mathrm{s}\, E_\mathrm{i}\, \widehat{\boldsymbol{s}}_\mathrm{r}\, e^{i\boldsymbol{k}_\mathrm{r}\cdot\boldsymbol{r}}, \qquad \boldsymbol{E}_{\mathrm{t,s}} = t_\mathrm{s}\, E_\mathrm{i}\, \widehat{\boldsymbol{s}}_\mathrm{t}\, e^{i\boldsymbol{k}_\mathrm{t}\cdot\boldsymbol{r}}, \tag{S6s}$$

where the time dependence, given by a common factor $e^{-i\omega t}$, with $\omega = k_0 c$ and the vacuum light velocity c, has been omitted. Note that $E_\mathrm{i} \in \mathbb{R}$ when the phase of $\boldsymbol{E}_\mathrm{i}$ is taken as reference. We then use Eq. (S6) to obtain the expression of $\boldsymbol{E}_\mathrm{exc}(x, y, z)$ we were after. $\boldsymbol{E}_\mathrm{exc}$ in medium 1 is the coherent superposition of the incident and reflected fields

$$\boldsymbol{E}_{1,\mathrm{p}}(\theta_\mathrm{i}, \varphi_\mathrm{i}) = \boldsymbol{E}_{\mathrm{i,p}} + \boldsymbol{E}_{\mathrm{r,p}} = E_\mathrm{i} \begin{bmatrix} \cos\theta_\mathrm{i} \cos\varphi_\mathrm{i}\, (e^{ik_{\mathrm{i},z}z} - r_\mathrm{p}\, e^{-ik_{\mathrm{i},z}z}) \\ \cos\theta_\mathrm{i} \sin\varphi_\mathrm{i}\, (e^{ik_{\mathrm{i},z}z} - r_\mathrm{p}\, e^{-ik_{\mathrm{i},z}z}) \\ -\sin\theta_\mathrm{i}\, (e^{ik_{\mathrm{i},z}z} + r_\mathrm{p}\, e^{-ik_{\mathrm{i},z}z}) \end{bmatrix} e^{i(k_{\mathrm{i},x}x + k_{\mathrm{i},y}y)}, \tag{S7p}$$

$$\boldsymbol{E}_{1,\mathrm{s}}(\theta_\mathrm{i}, \varphi_\mathrm{i}) = \boldsymbol{E}_{\mathrm{i,s}} + \boldsymbol{E}_{\mathrm{r,s}} = E_\mathrm{i} \begin{bmatrix} -\sin\varphi_\mathrm{i} \\ \cos\varphi_\mathrm{i} \\ 0 \end{bmatrix} \left(e^{ik_{\mathrm{i},z}z} + r_\mathrm{s}\, e^{-ik_{\mathrm{i},z}z}\right) e^{i(k_{\mathrm{i},x}x + k_{\mathrm{i},y}y)} \tag{S7s}$$

whereas $\boldsymbol{E}_\mathrm{exc}$ in medium 2 coincides with the transmitted field

$$\boldsymbol{E}_{2,\mathrm{p}}(\theta_\mathrm{i}, \varphi_\mathrm{i}) = \boldsymbol{E}_{\mathrm{t,p}} = t_\mathrm{p} E_\mathrm{i} \begin{bmatrix} \cos\theta_\mathrm{t} \cos\varphi_\mathrm{i} \\ \cos\theta_\mathrm{t} \sin\varphi_\mathrm{i} \\ -\sin\theta_\mathrm{t} \end{bmatrix} e^{i\boldsymbol{k}_\mathrm{t}\cdot\boldsymbol{r}}, \tag{S8p}$$

$$\boldsymbol{E}_{2,\mathrm{s}}(\theta_\mathrm{i}, \varphi_\mathrm{i}) = \boldsymbol{E}_{\mathrm{t,s}} = t_\mathrm{s} E_\mathrm{i} \begin{bmatrix} -\sin\varphi_\mathrm{i} \\ \cos\varphi_\mathrm{i} \\ 0 \end{bmatrix} e^{i\boldsymbol{k}_\mathrm{t}\cdot\boldsymbol{r}}. \tag{S8s}$$

We have highlighted that the fields (S7) and (S8) depend on the direction of incidence solely, as all other variables can be expressed as a function of $(\theta_\mathrm{i}, \varphi_\mathrm{i})$ via the relations between angles reported above. Eq. (S8) holds as well for total internal reflection (TIR), which occurs for $n_1 > n_2$ and $\theta_\mathrm{i} > \theta_\mathrm{c} = \arcsin(n_2/n_1)$. In this case $\theta_\mathrm{t} = n_2/n_1$ is a complex number and $k_{\mathrm{t},z} = -k_\mathrm{t} \cos\theta_\mathrm{t}$ becomes purely imaginary: The resulting real exponential in Eq. (S8) describes an evanescent decay of the field moving away from the interface.

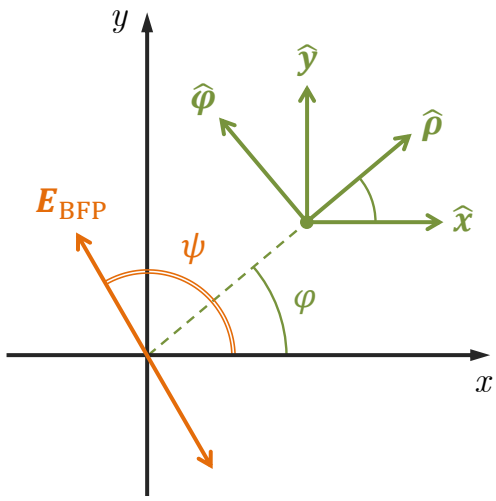

Figure S2. The BFP of the condenser is represented. $(\hat{\boldsymbol{x}}, \hat{\boldsymbol{y}})$ and $(\hat{\boldsymbol{\rho}}, \hat{\boldsymbol{\varphi}})$ are the basis versors of Cartesian and cylindrical coordinates respectively. The linearly polarized electric field $\boldsymbol{E}_{\mathrm{BFP}}$ forms an angle $\psi \in [0, \pi)$ with $\hat{\boldsymbol{x}}$.

B. Unpolarized and linearly polarized illumination

For unpolarized light, the p and s components of $\boldsymbol{E}_{\mathrm{exc}}$, $\boldsymbol{E}_{\mathrm{p}}$ and $\boldsymbol{E}_{\mathrm{s}}$, have the same amplitude and no phase relation. Accordingly, the expression of $\boldsymbol{E}_{\mathrm{exc}}$ given by Eq. (S7) and Eq. (S8) was used for simulating the optical cross-sections under unpolarized illumination of the gold and polystyrene spheres investigated in the paper. However, using polarized light is often useful, e. g. to study the optical properties of anisotropic NanOs such as the gold rods investigated in the paper. Under polarized illumination, $\boldsymbol{E}_{\mathrm{exc}}$ is a coherent superposition of $\boldsymbol{E}_{\mathrm{p}}$ and $\boldsymbol{E}_{\mathrm{s}}$, with coefficients depending on the direction of incidence. Let us derive the analytical form of the coefficients for linearly polarized illumination.

In our experiments, a linear polarization state can be created in the back focal plane (BFP) of the condenser lens; the azimuth ψ identifies the illumination direction as in Fig. S2. In terms of the Cartesian unit vectors, the electric field in the BFP is

$$\boldsymbol{E}_{\mathrm{BFP}} = [\hat{\boldsymbol{x}} \cos\psi + \hat{\boldsymbol{y}} \sin\psi]\, E_{\mathrm{i}}\, e^{-ik_0 z}. \tag{S9}$$

The illumination intensity is assumed to be homogeneous over the BFP, so that $\boldsymbol{E}_{\mathrm{BFP}}$ is independent of the position (ρ, φ) in the plane. As shown in Fig. S2, the basis unit vectors of Cartesian and cylindrical coordinates are related by a rotation around $\hat{\boldsymbol{z}}$ by the angle φ represented by the rotation matrix $\boldsymbol{R}_{\hat{\boldsymbol{z}}}(\varphi)$

$$\begin{bmatrix} \hat{\boldsymbol{x}} \\ \hat{\boldsymbol{y}} \end{bmatrix} = \boldsymbol{R}_{\hat{\boldsymbol{z}}}(-\varphi) \begin{bmatrix} \hat{\boldsymbol{\rho}} \\ \hat{\boldsymbol{\varphi}} \end{bmatrix} = \begin{bmatrix} \hat{\boldsymbol{\rho}} \cos\varphi - \hat{\boldsymbol{\varphi}} \sin\varphi \\ \hat{\boldsymbol{\rho}} \sin\varphi + \hat{\boldsymbol{\varphi}} \cos\varphi \end{bmatrix}. \tag{S10}$$

$\boldsymbol{E}_{\mathrm{BFP}}$ can be thereby expressed in terms of the cylindrical versors

$$\boldsymbol{E}_{\mathrm{BFP}}(\varphi) = \left[\hat{\boldsymbol{\rho}} \cos(\psi - \varphi) + \hat{\boldsymbol{\varphi}} \sin(\psi - \varphi)\right] E_{\mathrm{i}}\, e^{-ik_0 z}\,. \tag{S11}$$

Let us now calculate $\boldsymbol{E}_{\mathrm{i}}$ corresponding to the direction of incidence $(\theta_{\mathrm{i}}, \varphi_{\mathrm{i}})$ in the front space of the condenser, where the spherical coordinates (r, θ, φ) are used. As illustrated by Fig. S1b,

the condenser focuses the collimated illumination onto the sample plane by converting the propagation direction $-\widehat{\boldsymbol{z}}$ into $-\widehat{\boldsymbol{r}}$, so that the resulting wavevector is $\boldsymbol{k}_\mathrm{i} = -k_\mathrm{i}\,\widehat{\boldsymbol{r}}(\theta_\mathrm{i},\varphi_\mathrm{i})$. Concurrently, the radial component $\widehat{\boldsymbol{\rho}}(\varphi_\mathrm{i})$ of the field is rotated into a polar one $\widehat{\boldsymbol{\theta}}(\theta_\mathrm{i},\varphi_\mathrm{i}) = \widehat{\boldsymbol{p}}_\mathrm{i}$, while the tangential component $\widehat{\boldsymbol{\varphi}}(\varphi_\mathrm{i}) = \widehat{\boldsymbol{s}}_\mathrm{i}$ is left unchanged. Thus

$$\begin{aligned}\boldsymbol{E}_\mathrm{i}(\theta_\mathrm{i},\varphi_\mathrm{i}) &= \Big[\cos(\psi-\varphi_\mathrm{i})\,\widehat{\boldsymbol{p}}_\mathrm{i} \;+\; \sin(\psi-\varphi_\mathrm{i})\,\widehat{\boldsymbol{s}}_\mathrm{i}\Big] E_\mathrm{i}\, e^{i\boldsymbol{k}_\mathrm{i}\cdot\boldsymbol{r}} \\ &= \cos(\psi-\varphi_\mathrm{i})\boldsymbol{E}_{\mathrm{i,p}} + \sin(\psi-\varphi_\mathrm{i})\boldsymbol{E}_{\mathrm{i,s}}\,,\end{aligned} \tag{S12}$$

namely, a coherent superposition of the p and s fields defined by Eq. (S6). Moreover, since the p and s components are not mixed upon reflection or transmission, an analogous expression holds for the reflected (i→r) and transmitted (i→t) waves.

We can eventually write via Eq. (S12) $\boldsymbol{E}_\mathrm{exc}$ above and below the interface, namely $\boldsymbol{E}_1 = \boldsymbol{E}_\mathrm{i} + \boldsymbol{E}_\mathrm{r}$ and $\boldsymbol{E}_2 = \boldsymbol{E}_\mathrm{t}$

$$\boldsymbol{E}_1(\theta_\mathrm{i},\varphi_\mathrm{i}) = \cos(\psi-\varphi_\mathrm{i})\,\boldsymbol{E}_{1,\mathrm{p}} + \sin(\psi-\varphi_\mathrm{i})\,\boldsymbol{E}_{1,\mathrm{s}} \tag{S13-1}$$

$$\boldsymbol{E}_2(\theta_\mathrm{i},\varphi_\mathrm{i}) = \cos(\psi-\varphi_\mathrm{i})\,\boldsymbol{E}_{2,\mathrm{p}} + \sin(\psi-\varphi_\mathrm{i})\,\boldsymbol{E}_{2,\mathrm{s}} \tag{S13-2}$$

with $\boldsymbol{E}_{1,\mathrm{p}}$, $\boldsymbol{E}_{1,\mathrm{s}}$ given by Eq. (S7) and and $\boldsymbol{E}_{2,\mathrm{p}}$, $\boldsymbol{E}_{2,\mathrm{s}}$ given by Eq. (S8). This expression for $\boldsymbol{E}_\mathrm{exc}$ was used for simulating the optical cross-sections under linearly polarized illumination of the gold rods investigated in the paper.

S.IV. ANALYTICAL DESCRIPTION OF THE MICROSCOPE ILLUMINATION

In many micro-spectroscopy experiments, such as those presented in this work, the sample is illuminated by a high NA condenser lens. The illumination NA range in BF modality is typically chosen to match the NA range of the microscope objective used, to provide the best diffraction-limited spatial resolution, while in DF modality the NA range of condenser and objective are chosen to have no overlap. Describing such excitation as a plane wave impinging perpendicularly onto the sample plane — a common approach to numerical modeling in the nanoplasmonics field — can provide insight as to the position and linewidth of the resonant modes of the investigated system, but is not suited to accurately calculate the measured cross-section magnitude. For example, the axial polarization component introduced by illumination at non-zero angles of incidence is not accounted for.

We will therefore develop in the following section S.IV A a mathematical description of the high NA, incoherent microscope illumination employed in our experiments. This description is an essential part of the method described in Sec. S.IV B to compute the cross-sections under microscope illumination, which are directly modeling the measurements. It is also used in the analytical model of scattering presented in Sec. S.V B, which we can use to calculate the scattering parameters of our quantitative method.

A. Angular dependence of the exciting power and intensity

Generally speaking, lens systems transform positions ($\rho_\mathrm{i}, \varphi_\mathrm{i}$ in cylindrical coordinates) in the back focal plane (BFP) to directions ($\theta_\mathrm{i}, \varphi_\mathrm{i}$ in spherical coordinates) impinging onto the front focal plane (FFP) as depicted in Fig. S1b — and vice versa. Consistently with the rest of this work, the subscript i stands for "incidence" and denotes coordinates and quantities related to the illumination. We consider axially-symmetric optical elements only, so that φ_i is conserved in the transformation. Aplanatic lens systems (aplanats) are of paramount importance for microscopy, because they are free of both off-axis coma and spherical aberration. An aplanat is defined by a specific relation between position in the BFP and angle of incidence in the FFP

$$\rho_\mathrm{i} = f\mathrm{NA}_\mathrm{i} = fn\sin\theta_\mathrm{i} \tag{S14}$$

where f is the effective focal length and n is the refractive index of the medium filling the FFP. In literature Eq. (S14) is referred to as *Abbe's sine condition*. In this work we assume that the condenser is an aplanat focusing the illumination onto the sample placed at the FFP: This is indeed an adequate description for a scientific-grade condenser lens such as that used in our experiments.

From a geometric point of view, an aplanat maps the flat wavefront of a collimated beam in the BFP into a hemispherical surface Σ (often called the *front principal "plane"*) of radius fn converging at the front focal point F as depicted in Fig. S3a. In our case, the illumination

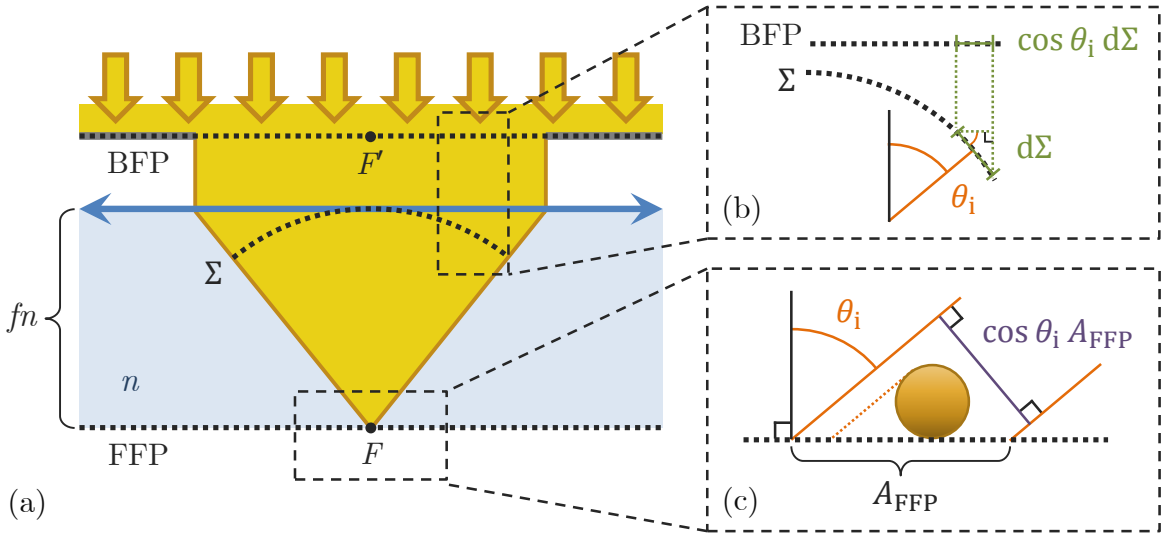

Figure S3. Sectional view of a typical Köhler illumination set-up for micro-spectroscopy experiments. The sketch depicts the main geometrical features associated with an aplanatic condenser lens (double arrow) discussed in the text. The angle of incidence θ_i in the magnified insets (b) and (c) is chosen larger that the illumination range in (a) for clarity.

originates from an incoherent source and therefore does not form a coherent wavefront in the BFP. Its coherence length in the BFP is given by the diffraction limit of the illuminated region in the FFP, which is an image of the field diaphragm in Köhler illumination. We use illuminated regions with sizes of about 300 μm, three orders of magnitude larger than the diffraction limited point spread function (PSF) size for the full condenser NA. Accordingly, the coherence length in the BFP is about three orders of magnitude smaller than the size of the BFP. We can therefore treat the coherence areas in the BFP as small elements of area $\mathrm{d}\Sigma = (fn)^2\,\mathrm{d}\Omega_\mathrm{i}$ corresponding to a well-defined direction of incidence $(\theta_\mathrm{i}, \varphi_\mathrm{i})$, of a plane wave propagating towards F. Note that the effective condenser focal length fn, in our apparatus 10.5 mm, is much larger than the illuminated region, so that the illumination in the BFP of the condenser is still collimated to a small angular range, in our case about 0.03 radians. The illumination impinging on the sample is then the *incoherent superposition* of these plane waves. Now, the small element of area $\mathrm{d}A_\mathrm{BFP}$ corresponding to $\mathrm{d}\Sigma$ shrinks towards the edges of the BFP, as illustrated by the geometrical construction in Fig. S3b. Equivalently, this result can be obtained as a consequence of the sine condition (S14)

$$\mathrm{d}A_\mathrm{BFP} = \rho_\mathrm{i}\,\mathrm{d}\rho_\mathrm{i}\,\mathrm{d}\varphi_\mathrm{i} = (fn)^2\cos\theta_\mathrm{i}\sin\theta_\mathrm{i}\,\mathrm{d}\theta_\mathrm{i}\,\mathrm{d}\varphi_\mathrm{i} = (fn)^2\cos\theta_\mathrm{i}\,\mathrm{d}\Omega_\mathrm{i} = \cos\theta_\mathrm{i}\,\mathrm{d}\Sigma\,. \tag{S15}$$

The factor thereby introduced is sometimes referred to as the *aplanatic apodization cosine*.

We want now to investigate the dependence on θ_i of the power $\mathrm{d}P_\mathrm{PW}$ and intensity $\mathrm{d}I_\mathrm{PW}$ carried by the plane waves (PW) in our description. With $\mathrm{d}\Sigma$ and $\mathrm{d}A_\mathrm{BFP}$ related via Eq. (S15), the same power crosses them by geometrical construction in a ray picture

$$\mathrm{d}P_\mathrm{PW} = \mathrm{d}P_\mathrm{BFP} = I_\mathrm{BFP}\,\mathrm{d}A_\mathrm{BFP} = I_\mathrm{BFP}\cos\theta_\mathrm{i}\,\mathrm{d}\Sigma \tag{S16}$$

where I_BFP is the illumination intensity over the BFP, which is assumed to be constant. Eq. (S16) shows that $\mathrm{d}P_\mathrm{PW}$ decreases as θ_i increases, ruled by the aplanatic apodization cosine.

Let us call A_FFP the illuminated region of the FFP. As discussed before, under the Köhler illumination scheme employed in our set-up, A_FFP is defined by the field aperture and is the same for all directions of incidence. This implies that the plane wave elements have a wavefront of size A_PW, which according to the geometry given in Fig. S3c is given by $A_\mathrm{PW} = \cos\theta_\mathrm{i} A_\mathrm{FFP}$, reduced compared to A_FFP by the *beam squeezing cosine*. This expression of A_PW can be used to calculate the intensity of the plane wave

$$\mathrm{d}I_\mathrm{PW} \equiv \frac{\mathrm{d}P_\mathrm{PW}}{A_\mathrm{PW}} = I_\mathrm{BFP}\frac{\mathrm{d}\Sigma}{A_\mathrm{FFP}} \tag{S17}$$

where the expression (S16) of $\mathrm{d}P_\mathrm{PW}$ has been substituted in the last equality. Eq. (S17) shows that $\mathrm{d}I_\mathrm{PW}$ is independent of the illumination direction: This is a non-trivial consequence of an exact compensation between the aplanatic apodization cosine and the beam squeezing cosine under the Köhler illumination scheme.

B. Angular averaging of the simulated cross-sections

In our numerical simulations, we compute the cross-section σ^{PW} under plane wave illumination (in this work we use superscripts consistently to indicate the illumination condition), obtained using the plane wave expressions of $\boldsymbol{E}_{\mathrm{exc}}$ derived in Sec. S.III. On the other hand, what is measured in micro-spectroscopy experiments is the cross-section under microscope (m) illumination σ^{m}. In this section, we will use the mathematical description of the microscope illumination developed in Sec. S.IV A to express σ^{m} in terms of σ^{PW}, to relate the simulated to the measured cross-sections.

Let us begin with the definition of the cross-section as the power removed from the exciting electromagnetic mode(s) by a given optical process divided by the incident intensity

$$\sigma^{\mathrm{m}} \equiv \frac{P^{\mathrm{m}}}{I_{\mathrm{FFP}}} = \frac{\int_{\mathrm{ill}} \sigma^{\mathrm{PW}}(\theta_{\mathrm{i}}, \varphi_{\mathrm{i}})\, \mathrm{d}I_{\mathrm{PW}}}{\int_{\mathrm{ill}} \cos\theta_{\mathrm{i}}\, \mathrm{d}I_{\mathrm{PW}}}. \tag{S18}$$

Importantly, referencing occurs with respect to the intensity I_{FFP} traversing the FFP, to reproduce the way $S_{\mathrm{bg}}^{\mathrm{BF}}$ is measured in experiments, where the microscope objective images the sample plane onto the sensor. In the second equality of Eq. (S18), power and intensity are expressed as the sum over the contributions of the plane waves within the illumination cone. Note that while the removed power is proportional to the plane wave intensity $\mathrm{d}I_{\mathrm{PW}}$, the corresponding reference intensity is proportional to the power $\mathrm{d}P_{\mathrm{PW}}$ traversing A_{FFP}, so that a $\cos\theta_{\mathrm{i}}$ factor appears at the denominator, see also Fig. S3c. Effectively, the way referencing is performed in experiments results in $\sigma^{\mathrm{m}} > \sigma^{\mathrm{PW}}$, as if the NanO shadow projected onto the FFP was measured (dashed orange line in Fig. S3c). By virtue of this analogy, we call the $\cos\theta_{\mathrm{i}}$ factor in Eq. (S18) the *long shadow cosine*.

$\mathrm{d}I_{\mathrm{PW}}$ given by Eq. (S17) can be rewritten using Eq. (S15) as

$$\mathrm{d}I_{\mathrm{PW}} = \frac{I_{\mathrm{BFP}}}{A_{\mathrm{FFP}}} \frac{\mathrm{d}A_{\mathrm{BFP}}}{\cos\theta_{\mathrm{i}}} = \frac{I_{\mathrm{BFP}}}{A_{\mathrm{FFP}}} (fn)^2\, \mathrm{d}\Omega_{\mathrm{i}} \tag{S19}$$

By substituting the first expression into Eq. (S18)

$$\sigma^{\mathrm{m}} = \frac{\int_{A_{\mathrm{i}}} [\sigma^{\mathrm{PW}}(\theta_{\mathrm{i}}, \varphi_{\mathrm{i}}) / \cos\theta_{\mathrm{i}}]\, \mathrm{d}A_{\mathrm{BFP}}}{\int_{A_{\mathrm{i}}} \mathrm{d}A_{\mathrm{BFP}}} = \left\langle \frac{\sigma^{\mathrm{PW}}}{\cos\theta_{\mathrm{i}}} \right\rangle_{A_{\mathrm{i}}} \tag{S20}$$

we obtain a formula of simple interpretation: σ^{m} is the average of σ^{PW}over the illuminated region A_{i} of the BFP, weighted by the inverse long shadow cosine to account for the experimental referencing to I_{FFP}. Now, since we compute σ^{PW} as a function of the direction of incidence, the integration must be recast over the angular variables using the last form of Eq. (S19)

$$\sigma^{\mathrm{m}} = \frac{\int_{\Omega_{\mathrm{i}}} \sigma^{\mathrm{PW}}(\theta_{\mathrm{i}}, \varphi_{\mathrm{i}})\, \mathrm{d}\Omega_{\mathrm{i}}}{\int_{\Omega_{\mathrm{i}}} \cos\theta_{\mathrm{i}}\, \mathrm{d}\Omega_{\mathrm{i}}} = \frac{\int_{\underline{\theta}_{\mathrm{i}}}^{\bar{\theta}_{\mathrm{i}}} \int_0^{2\pi} \sigma^{\mathrm{PW}}(\theta_{\mathrm{i}}, \varphi_{\mathrm{i}}) \sin\theta_{\mathrm{i}}\, \mathrm{d}\theta_{\mathrm{i}}\, \mathrm{d}\varphi_{\mathrm{i}}}{\int_{\underline{\theta}_{\mathrm{i}}}^{\bar{\theta}_{\mathrm{i}}} \int_0^{2\pi} \cos\theta_{\mathrm{i}} \sin\theta_{\mathrm{i}}\, \mathrm{d}\theta_{\mathrm{i}}\, \mathrm{d}\varphi_{\mathrm{i}}}. \tag{S21}$$

$\sigma^{\mathrm{PW}}(\theta_{\mathrm{i}}, \varphi_{\mathrm{i}})$ is a discrete set of data, interpolated with constant steps $\Delta\theta_{\mathrm{i}}$ and $\Delta\varphi_{\mathrm{i}}$ from the sparse simulated values. The integral (S21) is therefore approximated by the discrete sum

$$\sigma^{\mathrm{m}}(\psi) \simeq \frac{\sum_{m,n} \sigma^{\mathrm{PW}}(\theta_{\mathrm{i},m}, \varphi_{\mathrm{i},n}, \psi) \sin\theta_{\mathrm{i},m}}{N \sum_m \cos\theta_{\mathrm{i},m} \sin\theta_{\mathrm{i},m}} \quad \text{with} \quad m \in 1 \dots M,\, n \in 1 \dots N \tag{S22}$$

where we have highlighted that, under linearly polarized illumination, the cross-sections depend on the polarization direction ψ in the BFP of the condenser defined as in Fig. S2. Under unpolarized illumination ($\nexists$), two incoherent plane waves having equal intensity and orthogonal polarization — say, p and s — correspond to each direction of incidence, so that $\sigma^{\mathrm{PW}} = (\sigma^{\mathrm{p}} + \sigma^{\mathrm{s}})/2$ and we have

$$\sigma^{\mathrm{m}}(\nexists) \simeq \frac{\sum_{m,n} \left[\sigma^{\mathrm{p}}(\theta_{\mathrm{i},m}, \varphi_{\mathrm{i},n}) + \sigma^{\mathrm{s}}(\theta_{\mathrm{i},m}, \varphi_{\mathrm{i},n})\right] \sin\theta_{\mathrm{i},m}}{2N \sum_m \cos\theta_{\mathrm{i},m} \sin\theta_{\mathrm{i},m}}. \tag{S23}$$

Often one can use the symmetries of the investigated system (excitation + NanO) to reduce the integration/summation domain in the formulae above. This is useful as it cuts the number of simulations required for averaging with a given accuracy, and hence the total computation time. In particular, symmetry with respect to the optical axis $\hat{\boldsymbol{z}}$ allows to reduce the domain of φ_{i}; let us illustrate this through a few, experimentally relevant examples. We assume the NanO has at least one mirror plane containing $\hat{\boldsymbol{z}}$, and orient the axes so that $\hat{\boldsymbol{x}}$ lies on such plane. If the NanO admits

- one mirror plane ($x = 0$), then the domain can be reduced to $\varphi_{\mathrm{i}} \in [0, \pi)$ for excitation polarized along $\hat{\boldsymbol{x}}$ or $\hat{\boldsymbol{y}}$, or unpolarized. The whole $\varphi_{\mathrm{i}} \in [0, 2\pi)$ domain must still be simulated for a generic exciting polarization. This is for instance the case of tetrahedra or sphere heterodimers.
- two orthogonal mirror planes ($x = 0$ and $y = 0$), then the domain can be reduced to $\varphi_{\mathrm{i}} \in [0, \pi)$ under a generic linearly polarized illumination, and to $\varphi_{\mathrm{i}} \in [0, \pi/2)$ for excitation polarized along $\hat{\boldsymbol{x}}$ or $\hat{\boldsymbol{y}}$, or else unpolarized. This is for instance the case of rods, cubes, and sphere homodimers.
- $\hat{\boldsymbol{z}}$ as a continuous axis of rotation, then $\sigma^{\mathrm{m}}(\psi) = \sigma^{\mathrm{m}}(\nexists)$, and any single value of φ_{i} ($N = 1$) can be used to compute Eq. (S23). This is for instance the case of spheres, disks lying flat on a substrate, and cones or pillars standing on a substrate.

Note that the presence of optical interfaces $\perp \hat{\boldsymbol{z}}$ is irrelevant for these symmetry considerations.

Carrying out the directional averaging just described at every simulated wavelength would be rather burdensome; therefore, in this work, we simulated the angular dependence $\sigma^{\mathrm{PW}}(\theta_{\mathrm{i}}, \varphi_{\mathrm{i}})$ for a single wavelength (at resonance, when present) and computed the factor $\sigma^{\mathrm{m}}/\sigma^{\mathrm{PW}}|_{\theta_{\mathrm{i}}=0}$. Then the full spectrum was simulated at normal incidence ($\theta_{\mathrm{i}} = 0$) only, and multiplied by this factor. This approach, whereby the directional response of the system is assumed to be independent of λ is applied throughout this work. Specifically, the scattering parameters η^l and ζ also are computed for a given form of $\boldsymbol{\alpha}$. In fact, if multiple modes of

different geometry were present in the same spectrum, the quantitative method would have to be applied separately to them (different angular scaling factor, and different scattering parameters).

Somewhat surprisingly, due to the long shadow effect described above, σ^{m} is larger than σ^{PW} even in the most symmetric case of a sphere surrounded by a homogeneous medium. Indeed, this system is isotropic so that σ^{PW} does not depend on $(\theta_{\mathrm{i}}, \varphi_{\mathrm{i}})$ and can be taken out of the integral (S21), yielding

$$\sigma^{\mathrm{m}} = \frac{2\pi\sigma^{\mathrm{PW}} \int_{\underline{\theta}_{\mathrm{i}}}^{\overline{\theta}_{\mathrm{i}}} \sin\theta_{\mathrm{i}}\, \mathrm{d}\theta_{\mathrm{i}}}{2\pi \int_{\underline{\theta}_{\mathrm{i}}}^{\overline{\theta}_{\mathrm{i}}} \cos\theta_{\mathrm{i}} \sin\theta_{\mathrm{i}}\, \mathrm{d}\theta_{\mathrm{i}}} = \frac{2\,\sigma^{\mathrm{PW}}}{\cos\underline{\theta}_{\mathrm{i}} + \cos\overline{\theta}_{\mathrm{i}}}\,. \tag{S24}$$

This formula was used for the gold spheres investigated in the paper. With the illumination ranges used ($\mathrm{NA}_{\mathrm{i}}^{\mathrm{BF}}$ from 0 to 0.95 corresponding to $\theta_{\mathrm{i}}^{\mathrm{BF}}$ from 0 to 38.7°; and $\mathrm{NA}_{\mathrm{i}}^{\mathrm{DF}}$ from 1.10 to 1.28 corresponding to $\theta_{\mathrm{i}}^{\mathrm{DF}}$ from 46.4 to 57.4°) one has $\sigma_{\mathrm{abs}}^{\mathrm{BF}} = 1.12\,\sigma_{\mathrm{abs}}^{\mathrm{PW}}$ and $\sigma_{\mathrm{sca}}^{\mathrm{DF}} = 1.63\,\sigma_{\mathrm{sca}}^{\mathrm{PW}}$ respectively. In a recent work [S4] we verified experimentally on absorption-dominated gold spheres the dependence of $\sigma_{\mathrm{ext}}^{\mathrm{m}}$ on the angular range of illumination predicted by Eq. (S24).

S.V. CALCULATION OF THE SCATTERING PARAMETERS

Eq. (7) of the paper express the cross-section amplitudes as functions of the experimental signals, and contain the *scattering parameters*

$$\eta^l \equiv \frac{P_{\mathrm{obj}}^l}{P_{\mathrm{sca}}^l} = \frac{P_{\mathrm{det}}^l(\theta_{\mathrm{obj}}, \pi)}{P_{\mathrm{det}}^l(0,\pi)} \quad \text{and} \quad \zeta \equiv \frac{P_{\mathrm{sca}}^{\mathrm{BF}}}{P_{\mathrm{sca}}^{\mathrm{DF}}} = \frac{P_{\mathrm{det}}^{\mathrm{BF}}(0,\pi)}{P_{\mathrm{det}}^{\mathrm{DF}}(0,\pi)} \tag{S25}$$

where $l \in [\mathrm{BF}, \mathrm{DF}]$ denotes the illumination modality. In Eq. (S25) the scattering parameters are expressed in terms of

$$P_{\mathrm{det}}^l(\underline{\theta}_{\mathrm{d}}, \overline{\theta}_{\mathrm{d}}) \equiv \int_{\Omega_{\mathrm{d}}} \mathcal{P}_{\mathrm{NO}}^l(\theta, \varphi)\, \mathrm{d}\Omega \tag{S26}$$

which is the power scattered within the solid angle of detection Ω_{d} defined in spherical coordinates by the angular ranges $\theta \in [\underline{\theta}_{\mathrm{d}}, \overline{\theta}_{\mathrm{d}}]$ and $\varphi \in [0, 2\pi)$ owing to the axial symmetry of our detection geometry. In Eq. (S26) $\mathcal{P}_{\mathrm{NO}}^l$ is the angular distribution of the power scattered by the NanO to the far-field. Note that in this work we reserve the calligraphic font $\mathcal{P}$ to angular power distributions (units W/sr), whereas integrated powers (units W) are indicated by the usual italic font P.

In general, $\mathcal{P}_{\mathrm{NO}}^l$ depends both on the electromagnetic excitation and on the optical response of the NanO. Writing an explicit form of excitation and response requires some assumptions, which are listed right before Eq. (10) of the paper. Nonetheless, the expressions of P_{det}^l, and hence of η^l and ζ, we derive in this section, still apply to many experimentally relevant cases. One assumption we make in our treatment is the *dipole approximation*, which is accurate in the electrostatic regime, where the NanO is much smaller than the excitation wavelength. Within this approximation, higher-order multipolar terms of the charge distribution induced

in the NanO are neglected, and only an electric dipole moment is considered. Schematically, our description of the scattering process consists of two steps: (i) a set of dipoles are excited at the NanO; (ii) these dipoles radiate. Now, (i) precedes (ii) and is independent from it, meaning that all interactions of the dipole with the field it radiates are neglected in this description. Firstly, this restricts the validity of these calculations to weak scatterers, consistent with the small-NanO limitation imposed by the dipole approximation. Secondly, in presence of an interface near the NanO, scattering of the reflected radiation is not taken into account. This is expected to be a suitable approximation for the measurements presented in this work, where the NanO is placed either in a homogeneous medium or at a moderately mismatched glass/air interface, creating only weak reflections of the scattered field.

Let us first present in Sec. S.V A some results on the radiation emitted by oscillating dipoles, which we will need in the following. In Sec. S.V B we will then carry out calculations for common types of NanOs.

A. Dipole radiation near a dielectric interface

Lukosz and Kunz have derived in a series of papers [S5–S8] the angular distribution $\mathcal{P}(\theta,\varphi)$ of the power radiated by an oscillating electric dipole $\boldsymbol{p}$ placed at a distance z_{NO} from a planar dielectric interface. We report here for convenience their results recast into the notation used throughout this work. The expressions have been simplified by assuming $z_{\mathrm{NO}}=0$, since in our experiments the NanO always lies on the substrate and is described as point-like in the electrostatic regime.

The geometry of the problem is the one shown in Fig. S1a, where $\boldsymbol{p}$ is placed in medium 2 and has an arbitrary direction described by the spherical angles (Θ,Φ). Following Ref. [S8] we define the emission angles θ_1 and θ_2 in media 1 and 2 relative to the z axis analogously to θ_{i} and θ_{t}, so that $\theta_{1,2}\in[0,\pi/2]$ and $n_1\sin\theta_1=n_2\sin\theta_2$. The corresponding angle $\theta\in[0,\pi]$ in standard spherical coordinates is thus $\theta=\theta_1$ in medium 1 and $\theta\equiv\pi-\theta_2$ in medium 2. In medium 1, the angular distribution of the power radiated with p and s polarization is

$$\mathcal{P}_{1,\mathrm{p}}(\theta_1,\varphi)=\frac{3}{2\pi}n^3\cos^2\theta_1\left[\frac{\cos\Theta\sin\theta_2+\sin\Theta\cos\theta_2\cos(\varphi-\Phi)}{\cos\theta_1+n\cos\theta_2}\right]^2 \tag{S27p}$$

$$\mathcal{P}_{1,\mathrm{s}}(\theta_1,\varphi)=\frac{3}{2\pi}n^3\cos^2\theta_1\left[\frac{\sin\Theta\sin(\varphi-\Phi)}{n\cos\theta_1+\cos\theta_2}\right]^2 \tag{S27s}$$

where $n\equiv n_1/n_2$ is the refractive index ratio of the interface. Eq. (S27) are replaced by

$$\mathcal{P}_{1,\mathrm{p}}(\theta_1,\varphi)=\frac{3}{2\pi}\frac{n^3}{n^2-1}\cos^2\theta_1\frac{n^2\cos^2\Theta\sin^2\theta_1+\sin^2\Theta\cos^2(\varphi-\Phi)(n^2\sin^2\theta_1-1)}{(n^2+1)\sin^2\theta_1-1} \tag{S28p}$$

$$\mathcal{P}_{1,\mathrm{s}}(\theta_1,\varphi)=\frac{3}{2\pi}\frac{n^3}{n^2-1}\cos^2\theta_1\sin^2\Theta\sin^2(\varphi-\Phi) \tag{S28s}$$

in the regime where evanescent plane waves in the dipole's near field are transmitted as plane waves into medium 1 — namely, for $n > 1$ and $\theta_1 > \theta_{1,\mathrm{c}} = \arcsin 1/n$.

In medium 2 the angular distribution of the radiated power is

$$\mathcal{P}_{2,\mathrm{p}}(\theta_2, \varphi) = \frac{3}{2\pi} \cos^2\theta_2 \left[\frac{n \cos\Theta \sin\theta_2 - \sin\Theta \cos\theta_1 \cos(\varphi - \Phi)}{\cos\theta_1 + n \cos\theta_2} \right]^2 \tag{S29p}$$

$$\mathcal{P}_{2,\mathrm{s}}(\theta_2, \varphi) = \frac{3}{2\pi} \cos^2\theta_2 \left[\frac{\sin\Theta \sin(\varphi - \Phi)}{n \cos\theta_1 + \cos\theta_2} \right]^2 \tag{S29s}$$

which are replaced by

$$\mathcal{P}_{2,\mathrm{p}}(\theta_2, \varphi) = \frac{3}{2\pi} \frac{1}{1-n^2} \cos^2\theta_2 \frac{n^4 \cos^2\Theta \sin^2\theta_2 + \sin^2\Theta \cos^2(\varphi - \Phi)(\sin^2\theta_2 - n^2)}{(n^2+1)\sin^2\theta_2 - n^2} \tag{S30p}$$

$$\mathcal{P}_{2,\mathrm{s}}(\theta_2, \varphi) = \frac{3}{2\pi} \frac{1}{1-n^2} \cos^2\theta_2 \sin^2\Theta \sin^2(\varphi - \Phi) \tag{S30s}$$

in the regime where the dipole radiation is totally internally reflected at the interface — namely, for $n < 1$ and $\theta_2 > \theta_{2,\mathrm{c}} = \arcsin n$. If the dipole is placed in medium 1 instead, the subscripts 1 and 2 must be exchanged in Eq. (S27)–(S30) as well as in the definition of n.

The overall power distribution $\mathcal{P}(\theta, \varphi) = \mathcal{P}_\mathrm{p} + \mathcal{P}_\mathrm{s}$ described by Eq. (S27)–(S30) is represented in Fig. S4 for an interface of glass with air, water, and index-matching immersion oil, and for dipoles having different orientations. Discontinuities of the distribution occur in the denser medium at the critical angle ($\theta_{1,\mathrm{c}} = 41.1°$ in air and $\theta_{1,\mathrm{c}} = 61.0°$ in water) as well as along the interface, where propagation is impeded. These plots highlight how significantly the directionality of the emission is affected by the presence of an interface, even at a moderate refractive index mismatch. Simple phenomenological methods used sometimes in literature such as the effective medium approximation are therefore inadequate for the quantitative analysis presented in this work.

Normalization of the radiated power distributions $\mathcal{P}(\theta, \varphi)$ is normalized to the total power radiated P_tot expressed in units of $P_\mathrm{iso} \equiv \lim_{z_\mathrm{NO}\to\infty} P_\mathrm{tot}(z_\mathrm{NO})$, i. e. the power radiated into an isotropic medium of refractive index n_2

$$\int_{4\pi} \mathcal{P}(\theta, \varphi)\, \mathrm{d}\Omega = \frac{P_\mathrm{tot}}{P_\mathrm{iso}}. \tag{S31}$$

P_iso is related to the total power P_vac radiated in vacuum ($n_2 = 1$) through

$$P_\mathrm{iso}(n_2) = n_2 \frac{p^2 \omega^4}{12\pi\varepsilon_0 c_0^3} = n_2 P_\mathrm{vac}. \tag{S32}$$

The quartic frequency dependence of Eq. (S32) is characteristic of dipole emission and rules the scattering spectrum of small dielectric particles, which display no material (e. g. plasmonic) resonances. Interestingly, Ref. [S6] demonstrates that the two dipoles with orientation $\perp$ and $\parallel$ to the interface radiate two orthogonal electromagnetic modes in the

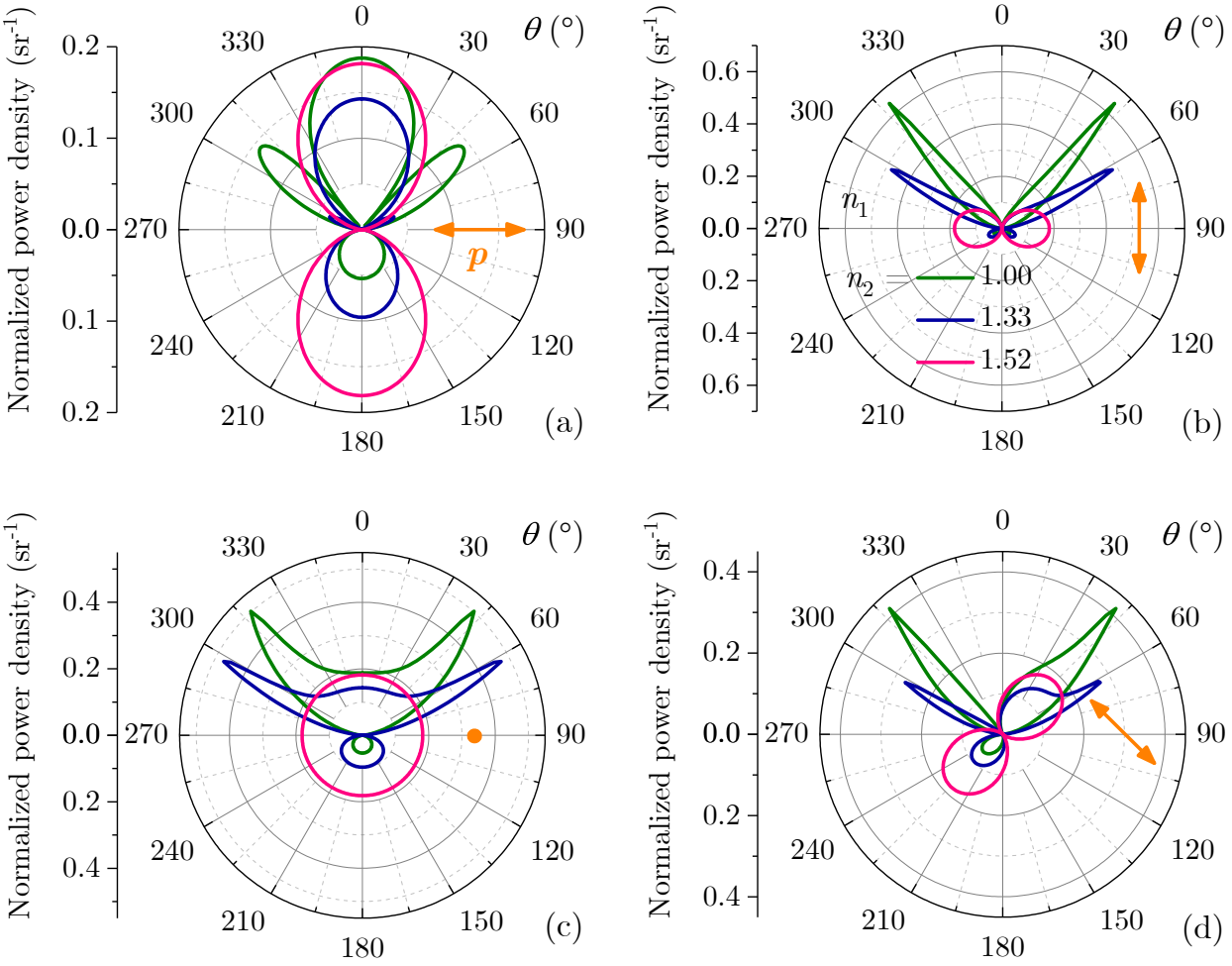

Figure S4. Normalized angular distribution $\mathcal{P}(\theta, 0) \times (P_{\rm iso}/P_{\rm vac})$ of the power radiated by an oscillating electric dipole placed at a planar $\theta = 90°$ dielectric interface. Medium 1 (above) and medium 2 (below) have refractive indices $n_1 = 1.52$ and n_2 as indicated in the legend of (b). The dipole is placed in medium 2 at a distance $z_{\rm NO} = 0$ from the interface. Note that the radial scale changes between panels. The orange arrows/dot indicate the dipole orientation:
(a) $\Theta = \pi/2$, $\Phi = 0$; (b) $\Theta = 0$;
(c) $\Theta = \pi/2$, $\Phi = \pi/2$; (d) $\Theta = \pi/4$, $\Phi = 0$.

far-field, so that the power emitted by an arbitrarily-oriented dipole can be decomposed into their independent contributions

$$\frac{P_{\rm tot}}{P_{\rm iso}}(n, \Theta) = p_{{\rm e},\perp}(n) \cos^2\Theta + p_{{\rm e},\parallel}(n) \sin^2\Theta \,. \tag{S33}$$

The coefficients in Eq. (S33) can be expanded into a Taylor series in powers of $4\pi z_{\rm NO}/\lambda_2$. In the limit $z_{\rm NO} = 0$ adopted in this work, we retain only the zero-order terms of the expansion,

whose coefficients are reported in Ref. [S5]

$$p_{\mathrm{m},\perp} = \frac{2}{5}\frac{n^5-1}{n^2-1}, \tag{S34a}$$

$$p_{\mathrm{m},\parallel} = \frac{1}{5}\frac{n^5-1}{n^2-1} - \frac{1}{2}\frac{n^2}{n+1}\left(1-\frac{3n}{n^2+1}\right) - \frac{3}{2}\frac{n^4\ln\left[(\sqrt{n^2+1}-n)(\sqrt{n^2+1}+1)/n\right]}{(n^2-1)(n^2+1)^{3/2}}, \tag{S34b}$$

$$p_{\mathrm{e},\perp} = \frac{2n^2}{n^2+1}p_{\mathrm{m},\parallel} - \frac{n^2-5}{n^2+1}p_{\mathrm{m},\perp} - 2, \tag{S34c}$$

$$p_{\mathrm{e},\parallel} = \frac{3\,p_{\mathrm{m},\perp} - p_{\mathrm{m},\parallel}}{n^2+1}, \tag{S34d}$$

where the m and e subscripts refer to a magnetic and an electric dipole respectively.

B. Parameters of some experimentally relevant nano-objects

In order to compute the integral (S26) we need first to break down $\mathcal{P}_{\text{NO}}$ into dipolar contributions. To begin with a simple description, one could represent the NanO as a single dipole $\boldsymbol{p}$ induced by the exciting field $\boldsymbol{E}_{\text{exc}}$

$$\boldsymbol{p} = \varepsilon_0\varepsilon_{\mathrm{m}}\boldsymbol{\alpha}\boldsymbol{E}_{\text{exc}} \tag{S35}$$

where $\boldsymbol{\alpha}$ is the polarizability tensor of the NanO and ε_{m} the permittivity of the embedding medium. Then, in terms of the dipolar power distribution introduced in the previous section

$$\mathcal{P}_{\text{NO}}(\theta,\varphi) \sim P_{\text{iso}}\,\mathcal{P}(\Theta,\Phi,\theta,\varphi) \tag{S36}$$

where $\mathcal{P}$ is the normalized angular distribution of the power scattered by $\boldsymbol{p}$. However, the microscope illumination cannot be accurately represented by a single analytical expression of $\boldsymbol{E}_{\text{exc}}$ due to its incoherent character — that is why the sign $\sim$ was used in Eq. (S36). As discussed in Sec. S.IV A, the microscope illumination is an incoherent superposition of plane waves, whose analytical form we derived in Sec. S.III. Consequently, the NanO is not just a single dipole, but rather a collection of dipoles oscillating with unrelated phases, and $\mathcal{P}_{\text{NO}}$ is the sum of the powers radiated by all the dipoles. The individual dipolar contributions have the form (S36) and their amplitude is proportional to $P_{\text{iso}} \propto p^2 \propto |\boldsymbol{E}_{\text{exc}}|^2$, that is, to the intensity of the exciting plane wave. Now, we found in S11 that the illumination intensity does not depend on θ_{i}, and therefore all the dipolar contributions have the same weight in the sum. In the dipole model we outlined, Eq. (S26) reads

$$P^l_{\text{det}}(\underline{\theta}^l_{\mathrm{i}},\overline{\theta}^l_{\mathrm{i}},\underline{\theta}_{\mathrm{d}},\overline{\theta}_{\mathrm{d}}) \propto \int_{\underline{\theta}^l_{\mathrm{i}}}^{\overline{\theta}^l_{\mathrm{i}}}\mathrm{d}\theta_{\mathrm{i}}\,\sin\theta_{\mathrm{i}}\int_0^{2\pi}\mathrm{d}\varphi_{\mathrm{i}}\int_{\underline{\theta}_{\mathrm{d}}}^{\overline{\theta}_{\mathrm{d}}}\mathrm{d}\theta\,\sin\theta\int_0^{2\pi}\mathrm{d}\varphi\;p^2(\theta_{\mathrm{i}},\varphi_{\mathrm{i}})\,\mathcal{P}(\theta_{\mathrm{i}},\varphi_{\mathrm{i}},\theta,\varphi)\,. \tag{S37}$$

where a constant factor $n_2\omega^4/(12\pi\varepsilon_0 c_0^3)$ in front of the integral has been omitted. In fact, the scattering parameters Eq. (S25) are defined as power ratios, which also renders them

independent of NanO size (within the dipole approximation) and composition (assuming an isotropic material response) – these properties affect only the absolute value of $P_{\rm det}$. In Eq. (S37) we highlighted that both the amplitude p and the orientation (Θ, Φ) of $\boldsymbol{p}$ depend on the direction of incidence of $\boldsymbol{E}_{\rm exc}$ given by $\theta_{\rm i} \in [\underline{\theta}_{\rm i}^l, \overline{\theta}_{\rm i}^l]$ and $\varphi_{\rm i} \in [0, 2\pi)$ owing to the axial symmetry of our illumination geometry.

Let us now consider the specific relevant scenario where all dipoles have a fixed orientation (Θ, Φ) regardless of the exciting polarization. This is relevant for instance at the longitudinal plasmon mode of an elongated NanO, where the dipoles are mostly excited along the longitudinal direction. Then $\mathcal{P}(\theta, \varphi)$ does not depend on $(\theta_{\rm i}, \varphi_{\rm i})$, and Eq. (S37) can be factorized into an *excitation integral* and a *detection integral*, $P_{\rm det}^l = L_{\rm exc}^l \, L_{\rm det}$, with

$$L_{\rm exc}^l(\underline{\theta}_{\rm i}^l, \overline{\theta}_{\rm i}^l) = \int_{\underline{\theta}_{\rm i}^l}^{\overline{\theta}_{\rm i}^l} {\rm d}\theta_{\rm i} \, \sin\theta_{\rm i} \int_0^{2\pi} {\rm d}\varphi_{\rm i} \, p^2(\theta_{\rm i}, \varphi_{\rm i}) \,, \tag{S38}$$

$$L_{\rm det}(\underline{\theta}_{\rm d}, \overline{\theta}_{\rm d}) = \int_{\underline{\theta}_{\rm d}}^{\overline{\theta}_{\rm d}} {\rm d}\theta \, \sin\theta \int_0^{2\pi} {\rm d}\varphi \, \mathcal{P}(\theta, \varphi) \,. \tag{S39}$$

$L_{\rm exc}^l$ is proportional to the total radiated power, and $L_{\rm det}$ is the power normalized to $P_{\rm iso}$, emitted within the detection range $\Omega_{\rm d}$. The excitation and detection parameters, given by Eq. (S25), can be written as

$$\zeta = \frac{L_{\rm exc}^{\rm BF}(\underline{\theta}_{\rm i}^{\rm BF}, \overline{\theta}_{\rm i}^{\rm BF})}{L_{\rm exc}^{\rm DF}(\underline{\theta}_{\rm i}^{\rm DF}, \overline{\theta}_{\rm i}^{\rm DF})} \quad \text{and} \quad \eta^{\rm BF} = \eta^{\rm DF} = \frac{L_{\rm det}(\theta_{\rm obj}, \pi)}{L_{\rm det}(0, \pi)} \tag{S40}$$

with $L_{\rm det}(0, \pi) = P_{\rm tot}/P_{\rm iso}$ given by Eq. (S33). In the rest of the section, the integrals (S37) or (S39)-(S39) are computed for some diagonal forms of $\boldsymbol{\alpha}$ corresponding to relevant symmetries of the resonant modes of NanOs.

1. Uniaxial polarizability parallel to the interface

Let us begin by considering a uniaxial $\boldsymbol{\alpha}$ parallel to the interface — say along x without loss of generality: $(\alpha_{xx}, \alpha_{yy}, \alpha_{zz}) = (\alpha, 0, 0)$. This describes well, for instance, the longitudinal resonant mode of elongated particles like *rods* lying on the substrate, as well as the bonding mode of *dimers*, which is linearly polarized along the particle separation. As a result of the anisotropy of $\boldsymbol{\alpha}$, only the x component of $\boldsymbol{E}_{\rm exc}$ excites dipoles of amplitude

$$p(\theta_{\rm i}, \varphi_{\rm i}) = \varepsilon_0 \varepsilon_{\rm m} \left| \boldsymbol{\alpha} \boldsymbol{E}_{\rm exc} \right| = \varepsilon_0 \varepsilon_{\rm m} \alpha \left| E_{2,x}(\theta_{\rm i}, \varphi_{\rm i}) \right| . \tag{S41}$$

The orientation of these dipoles is $(\Theta = \pi/2, \Phi = 0)$ regardless of $(\theta_{\rm i}, \varphi_{\rm i})$, and therefore we can use the separated form (S38)-(S39) of $P_{\rm det}^l$. Substituting the expression of $E_{2,x}$ given by

Eq. (S8) and Eq. (S13-2), the excitation integral (S38) reads

$$L^l_{\mathrm{exc}}(\psi) \propto \int_{\underline{\theta}^l_{\mathrm{i}}}^{\overline{\theta}^l_{\mathrm{i}}} \mathrm{d}\theta_{\mathrm{i}}\ \sin\theta_{\mathrm{i}} \int_0^{2\pi} \mathrm{d}\varphi_{\mathrm{i}} \left| t_{\mathrm{p}} \cos\theta_{\mathrm{t}} \cos\varphi_{\mathrm{i}} \cos(\psi-\varphi_{\mathrm{i}}) - t_{\mathrm{s}} \sin\varphi_{\mathrm{i}} \sin(\psi-\varphi_{\mathrm{i}}) \right|^2$$
$$= \frac{\pi}{2} \int_{\underline{\theta}^l_{\mathrm{i}}}^{\overline{\theta}^l_{\mathrm{i}}} \mathrm{d}\theta_{\mathrm{i}}\ \sin\theta_{\mathrm{i}} \left\{ \left| t_{\mathrm{p}} \cos\theta_{\mathrm{t}} \right|^2 + \left| t_{\mathrm{s}} \right|^2 + \frac{\cos 2\psi}{2} \left| t_{\mathrm{p}} \cos\theta_{\mathrm{t}} + t_{\mathrm{s}} \right|^2 \right\} \tag{S42}$$

with an explicit dependence on the linear polarization ψ of the excitation in the BFP of the condenser. Note that t_{p}, t_{s}, and θ_{t} in the integrand of Eq. (S42) are all functions of θ_{i}, given by Eq. (S5) and Snell's law respectively. We have omitted the constant factor $(\varepsilon_0 \varepsilon_{\mathrm{m}} \alpha E_{\mathrm{i}})^2$ in front of the integral since we will take a ratio of this expression: In fact, $\zeta(\psi)$ is obtained by substituting Eq. (S42) into Eq. (S40).

The detection integral (S39) is computed via Eq. (S29) and (S30), as collection occurs only in medium 2

$$L_{\mathrm{det}}(0, \alpha_{\mathrm{obj}}) = 4 \int_0^{\alpha_{\mathrm{obj}}} \mathrm{d}\theta_2\ \sin\theta_2 \int_0^{\pi/2} \mathrm{d}\varphi\ \mathcal{P}_2(\theta_2, \varphi) \Big|_{\substack{\Theta=\pi/2 \\ \Phi=0}}. \tag{S43}$$

The fourfold symmetry (with respect to the $x = 0$ and $y = 0$ planes) of $\mathcal{P}_2$ has been exploited to reduce the azimuth integration range to $\varphi \in [0, \pi/2]$; these symmetry considerations are useful in order to reduce the time required for numerical integration. Note that the integration range of L_{det} has changed from $[\theta_{\mathrm{obj}}, \pi]$ to $[0, \alpha_{\mathrm{obj}}]$ because the integration now runs over θ_2 instead of θ — see Fig. S1b for the definition of these angles. $\eta^{\mathrm{BF}} = \eta^{\mathrm{DF}}$ is computed by substituting Eq. (S43) to the numerator of Eq. (S40), while the denominator is is $P_{\mathrm{tot}}/P_{\mathrm{iso}}\Big|_{\Theta=\pi/2} = p_{\mathrm{e},\perp}$, which is given by Eq. (S34).

The expressions of ζ and η^l we just derived were used for the quantitative analysis of the gold rods investigated in the paper.

Unpolarized illumination While η^l is independent of the excitation for this choice of $\boldsymbol{\alpha}$, $\zeta(\psi)$ depends on the polarization state in the BFP of the condenser. Let us then compute $\zeta(\nexists)$ under unpolarized illumination. The incoherent p and s components of $\boldsymbol{E}_{\mathrm{exc}}$ excite two orthogonal sets of dipoles which yield an independent contribution to the total radiated power, so that the detection integral (S38) reads

$$L^l_{\mathrm{exc}}(\nexists) = \int_{\underline{\theta}^l_{\mathrm{i}}}^{\overline{\theta}^l_{\mathrm{i}}} \mathrm{d}\theta_{\mathrm{i}}\ \sin\theta_{\mathrm{i}} \int_0^{2\pi} \mathrm{d}\varphi_{\mathrm{i}} \left\{ p_{\mathrm{p}}^2 + p_{\mathrm{s}}^2 \right\}. \tag{S44}$$

The two dipole moments in Eq. (S44) have amplitude $p_{\mathrm{p}} = \varepsilon_0 \varepsilon_{\mathrm{m}} \alpha |E_{2,\mathrm{p},x}|$ and $p_{\mathrm{s}} = \varepsilon_0 \varepsilon_{\mathrm{m}} \alpha |E_{2,\mathrm{s},x}|$. Using the expressions (S8) for the fields (with amplitude $E_{\mathrm{i}}/\sqrt{2}$ instead of E_{i} since each component carries half of the total incident intensity) one finds

$$L^l_{\mathrm{exc}}(\nexists) = \frac{\pi}{2} \int_{\underline{\theta}^l_{\mathrm{i}}}^{\overline{\theta}^l_{\mathrm{i}}} \mathrm{d}\theta_{\mathrm{i}}\ \sin\theta_{\mathrm{i}} \left\{ \left| t_{\mathrm{p}} \cos\theta_{\mathrm{t}} \right|^2 + \left| t_{\mathrm{s}} \right|^2 \right\} \tag{S45}$$

namely Eq. (S42) without the ψ-dependent term, which corresponds to interference between the p- and s-excited radiation. Since this term disappears for $\psi = \pi/4$ one has

$$L^l_{\mathrm{exc}}(\not\psi) = L^l_{\mathrm{exc}}(\pi/4) \quad \Longrightarrow \quad \zeta(\not\psi) \equiv \frac{L^{\mathrm{BF}}_{\mathrm{exc}}(\not\psi)}{L^{\mathrm{DF}}_{\mathrm{exc}}(\not\psi)} = \zeta(\pi/4)\,. \tag{S46}$$

Although one has $L^l_{\mathrm{exc}}(\pi/4) = \frac{1}{2}\left[L^l_{\mathrm{exc}}(\psi) + L^l_{\mathrm{exc}}(\psi+\pi/2)\right]$, we emphasize that in general

$$\zeta(\pi/4) = \frac{\frac{1}{2}\left[L^{\mathrm{BF}}_{\mathrm{exc}}(\psi) + L^{\mathrm{BF}}_{\mathrm{exc}}(\psi+\pi/2)\right]}{\frac{1}{2}\left[L^{\mathrm{DF}}_{\mathrm{exc}}(\psi) + L^{\mathrm{DF}}_{\mathrm{exc}}(\psi+\pi/2)\right]} \neq \frac{1}{2}\Big[\zeta(\psi) + \zeta(\psi+\pi/2)\Big] \tag{S47}$$

and in particular for unpolarized illumination $\zeta(\not\psi) \neq \Big[\zeta(0) + \zeta(\pi/2)\Big]/2$.

Homogeneous environment In the special case $n = 1$ representing a homogeneous optical environment, a closed-form expression of the scattering parameters can be derived. This scenario is of practical interest, as it corresponds to a NanO either covered by a fluid matching the refractive index of the substrate, or embedded in a solid matrix, or suspended within an optical trap. For $n = 1$ one has $t_{\mathrm{p}} = t_{\mathrm{s}} = 1$ and $\theta_{\mathrm{t}} = \theta_{\mathrm{i}}$, so that Eq. (S42) simplifies to

$$\begin{aligned} L^l_{\mathrm{exc}}(\psi) &\propto \int_{\underline{\theta}^l_{\mathrm{i}}}^{\overline{\theta}^l_{\mathrm{i}}} \mathrm{d}\theta_{\mathrm{i}}\ \sin\theta_{\mathrm{i}} \left\{ \cos^2\theta_{\mathrm{i}} + 1 + \frac{\cos 2\psi}{2}\Big(\cos\theta_{\mathrm{i}} + 1\Big)^2 \right\} \\ &= \left[\frac{\cos^3\theta_{\mathrm{i}}}{3} + \cos\theta_{\mathrm{i}} + \frac{\cos 2\psi}{6}\Big(\cos\theta_{\mathrm{i}} + 1\Big)^3 \right]_{\overline{\theta}^l_{\mathrm{i}}}^{\underline{\theta}^l_{\mathrm{i}}}; \end{aligned} \tag{S48}$$

note that the extrema in the final expression are inverted with respect to the integral. As for η^l, the denominator is $P_{\mathrm{tot}}/P_{\mathrm{iso}}\Big|_{n=1} = 1$ since there is no interface now. The numerator is the integral of $\mathcal{P}_2$ in a homogeneous environment, given by Eq. (S29) for $n = 1$ and $\theta_1 = \theta_2$

$$\begin{aligned} \eta^l =& L_{\mathrm{det}}(0, \alpha_{\mathrm{obj}}) \\ =& \int_0^{\alpha_{\mathrm{obj}}} \mathrm{d}\theta_2\ \sin\theta_2 \int_0^{2\pi} \mathrm{d}\varphi\ \frac{3}{8\pi}\Big\{ \cos^2\theta_2 \cos^2\varphi + \sin^2\varphi \Big\} \\ =& \frac{1}{8}\left(4 - 3\cos\alpha_{\mathrm{obj}} - \cos^3\alpha_{\mathrm{obj}}\right). \end{aligned} \tag{S49}$$

2. *Uniaxial polarizability perpendicular to the interface*

$(\alpha_{xx}, \alpha_{yy}, \alpha_{zz}) = (0, 0, \alpha)$ describes well, for instance, the longitudinal mode of *pillars* or *cones* standing on a substrate. Reasoning along the same lines as in Sec. S.V B 1, one has $p = \varepsilon_0\varepsilon_{\mathrm{m}}\alpha\,|E_{2,z}|$ and the excitation integral reads

$$L^l_{\mathrm{exc}} \propto \pi \int_{\underline{\theta}^l_{\mathrm{i}}}^{\overline{\theta}^l_{\mathrm{i}}} \mathrm{d}\theta_{\mathrm{i}}\ \sin\theta_{\mathrm{i}} \left| t_{\mathrm{p}} \sin\theta_{\mathrm{t}} \right|^2 \tag{S50}$$

where we have exploited the axial symmetry with respect to $\hat{\boldsymbol{z}}$ for the integration over φ_{i}. Similarly, the detection integral is

$$L_{\mathrm{det}}(0, \alpha_{\mathrm{obj}}) = 2\pi \int_0^{\alpha_{\mathrm{obj}}} \mathrm{d}\theta_2\ \sin\theta_2\, \mathcal{P}_{2,\mathrm{p}}(\theta_2, \varphi)\Big|_{\Theta=0} \tag{S51}$$

as $\mathcal{P}_{2,\mathrm{s}} \propto \sin^2\Theta$ vanishes for $\Theta = 0$ along with the φ dependence of $\mathcal{P}_{2,\mathrm{p}}$, see Eq. (S29) and Eq. (S30). ζ and η^l are computed by substituting the integrals (S50) and (S51) into Eq. (S40), while the denominator of η^l is $P_{\mathrm{tot}}/P_{\mathrm{iso}}\big|_{\Theta=0} = p_{\mathrm{e},\parallel}$ given by Eq. (S34).

For axially-symmetric modes like the ones considered in this and the next two sections, the powers in the definition (S25) of the scattering parameters do not depend on ψ. Therefore, ζ and η^l are the same for every exciting polarization as well as for unpolarized illumination. Indeed, the latter case is computed by averaging any two orthogonal polarization directions as done in Eq. (S46).

Homogeneous environment With considerations analogous to Sec. S.V B 1, the integrals (S50) and (S51) simplify to

$$L^l_{\mathrm{exc}} \propto \int_{\underline{\theta}^l_{\mathrm{i}}}^{\overline{\theta}^l_{\mathrm{i}}} \mathrm{d}\theta_{\mathrm{i}}\, \sin^3\theta_{\mathrm{i}} = \left[\frac{\cos^3\theta_{\mathrm{i}}}{3} - \cos\theta_{\mathrm{i}}\right]_{\underline{\theta}^l_{\mathrm{i}}}^{\overline{\theta}^l_{\mathrm{i}}}, \tag{S52}$$

$$\eta^l = L_{\mathrm{det}}(0, \alpha_{\mathrm{obj}}) = 2\pi \int_0^{\alpha_{\mathrm{obj}}} \mathrm{d}\theta_2\, \sin\theta_2\, \frac{3}{8\pi} \sin^2\theta_2 = \frac{1}{4}\left(2 - 3\cos\alpha_{\mathrm{obj}} + \cos^3\alpha_{\mathrm{obj}}\right). \tag{S53}$$

3. Isotropic planar polarizability parallel to the interface

The plasmonic resonance of a thin *disc* lying on the substrate, or the transverse mode of a *rod* standing on it, is described well by $(\alpha_{xx}, \alpha_{yy}, \alpha_{zz}) = (\alpha, \alpha, 0)$. One then has $p = \varepsilon_0\varepsilon_{\mathrm{m}}\alpha\sqrt{|E_{2,x}|^2 + |E_{2,y}|^2}$ and ζ is computed using

$$L^l_{\mathrm{exc}} \propto 2\pi \int_{\underline{\theta}^l_{\mathrm{i}}}^{\overline{\theta}^l_{\mathrm{i}}} \mathrm{d}\theta_{\mathrm{i}}\, \sin\theta_{\mathrm{i}} \left\{\left|t_{\mathrm{p}}\cos\theta_{\mathrm{t}}\right|^2 + \left|t_{\mathrm{s}}\right|^2\right\}. \tag{S54}$$

Not surprisingly, this result differs only by a constant factor from $L_{\mathrm{exc}}(\nleftrightarrow)$ calculated for $(\alpha_{xx}, \alpha_{yy}, \alpha_{zz}) = (\alpha, 0, 0)$, which is given by Eq. (S42) without the polarization-dependent term. η^l on the other hand is the same found for $(\alpha_{xx}, \alpha_{yy}, \alpha_{zz}) = (\alpha, 0, 0)$: In fact, for $\Theta = \pi/2$ the azimuthal orientation of the dipole is irrelevant for η^l due to the axial symmetry of the collection.

Homogeneous environment In accordance with the considerations just made for the general case, ζ is calculated using Eq. (S48) without the polarization-dependent term and η^l is given by Eq. (S49).

4. Isotropic polarizability

The isotropic optical response of a *sphere* is described by a scalar polarizability α. This case is inherently more complicated than the previous ones, inasmuch as the direction of the dipoles is not fixed: $\boldsymbol{p} = \varepsilon_0\varepsilon_{\mathrm{m}}\alpha\boldsymbol{E}_2(\theta_{\mathrm{i}}, \varphi_{\mathrm{i}})$. Therefore $\mathcal{P}(\theta, \varphi)$ depends on $(\theta_{\mathrm{i}}, \varphi_{\mathrm{i}})$ via (Θ, Φ), and the integral (S37) cannot be separated into excitation and detection parts as in the

previous cases. As discussed above, when $\hat{\boldsymbol{z}}$ is an axis of symmetry of the object, ζ and η^l do not depend on the exciting polarization: Calculations in this case are simplified by assuming unpolarized illumination. Indeed, once the symmetry breaking introduced by a linear polarization is removed, the whole problem (excitation + NanO) has axial symmetry, and therefore we can limit ourselves to consider a single plane of incidence.

Choosing then $\varphi_\mathrm{i} = 0$ without loss of generality, $\boldsymbol{E}_\mathrm{exc} = \boldsymbol{E}_2$ given by Eq. (S8) reduces to

$$\boldsymbol{E}_{2,\mathrm{p}}(\theta_\mathrm{i}, 0) = t_\mathrm{p} \frac{E_\mathrm{i}}{\sqrt{2}} \begin{bmatrix} \cos\theta_\mathrm{t} \\ 0 \\ -\sin\theta_\mathrm{t} \end{bmatrix} e^{i\boldsymbol{k}_\mathrm{t}\cdot\boldsymbol{r}}, \tag{S55p}$$

$$\boldsymbol{E}_{2,\mathrm{s}}(\theta_\mathrm{i}, 0) = t_\mathrm{s} \frac{E_\mathrm{i}}{\sqrt{2}} \begin{bmatrix} 0 \\ 1 \\ 0 \end{bmatrix} e^{i\boldsymbol{k}_\mathrm{t}\cdot\boldsymbol{r}}. \tag{S55s}$$

We emphasize that for unpolarized illumination $\boldsymbol{E}_{2,\mathrm{p}}$ and $\boldsymbol{E}_{2,\mathrm{s}}$ are incoherent, and therefore $\boldsymbol{E}_2$ is not their sum. They excite two incoherent dipoles of amplitude

$$p_\mathrm{p} = \varepsilon_0 \varepsilon_\mathrm{m} \alpha \left|\boldsymbol{E}_{2,\mathrm{p}}\right| \propto \left|t_\mathrm{p}\right| \quad \text{and} \quad p_\mathrm{s} = \varepsilon_0 \varepsilon_\mathrm{m} \alpha \left|\boldsymbol{E}_{2,\mathrm{s}}\right| \propto \left|t_\mathrm{s}\right|. \tag{S56}$$

The integrand in Eq. (S37) is thus the sum of the powers radiated by the p- and s-polarized dipoles

$$P^l_\mathrm{det} \propto 2 \int_{\underline{\theta}^l_\mathrm{i}}^{\overline{\theta}^l_\mathrm{i}} \mathrm{d}\theta_\mathrm{i}\, \sin\theta_\mathrm{i} \int_{\underline{\theta}_\mathrm{d}}^{\overline{\theta}_\mathrm{d}} \mathrm{d}\theta\, \sin\theta \int_0^\pi \mathrm{d}\varphi \left\{ \left|t_\mathrm{p}\right|^2 \mathcal{P}(\theta,\varphi)\Big|_{\substack{\Theta=\pi/2-\mathrm{Re}(\theta_\mathrm{t}) \\ \Phi=0}} + \left|t_\mathrm{s}\right|^2 \mathcal{P}(\theta,\varphi)\Big|_{\substack{\Theta=\pi/2 \\ \Phi=\pi/2}} \right\} \tag{S57}$$

where $\mathcal{P}(\theta,\varphi)$ has only a twofold symmetry with respect to φ because $\boldsymbol{p}_\mathrm{p}$ is not parallel to the interface. The real part appearing in the definition of Θ for the p dipole (hence Θ_p) fixes $\boldsymbol{p}_\mathrm{p} \parallel \hat{\boldsymbol{z}}$ for $\theta_\mathrm{i} \geq \theta_{1,\mathrm{c}}$, where only the imaginary part of θ_t varies; we will discuss soon the reasons and the effects of this approximation. Eventually, ζ and η^l are computed by substituting Eq. (S57) into Eq. (S25). Note that the explicit expressions (S29)–(S30) of $\mathcal{P}$ have to be evaluated only for the denominator of η^l; all other powers in Eq. (S25) are integrals over $\Omega_\mathrm{d} = 4\pi$ and can be simplified using Eq. (S31). These expressions of ζ and η^l were used for the quantitative analysis of the gold and polystyrene spheres investigated in the paper.

To summarize, differently from the previous cases, for a sphere $\mathcal{P}_\mathrm{NO}$ depends on the illumination. This is illustrated by Fig. S5, where the detection parameter is computed using a 1° wide illumination cone. A discontinuity of $\eta^{1^\circ}(\theta_\mathrm{i})$ at $\theta_\mathrm{i} = \theta_{1,\mathrm{c}}$ separates two regimes:

- For $\theta_\mathrm{i} < \theta_{1,\mathrm{c}}$ one has $\Theta_\mathrm{p} = \pi/2 - \theta_\mathrm{t}$; as the p dipole progressively aligns to $-\hat{\boldsymbol{z}}$ (where the objective is placed) less scattering is collected, see Fig. S4.

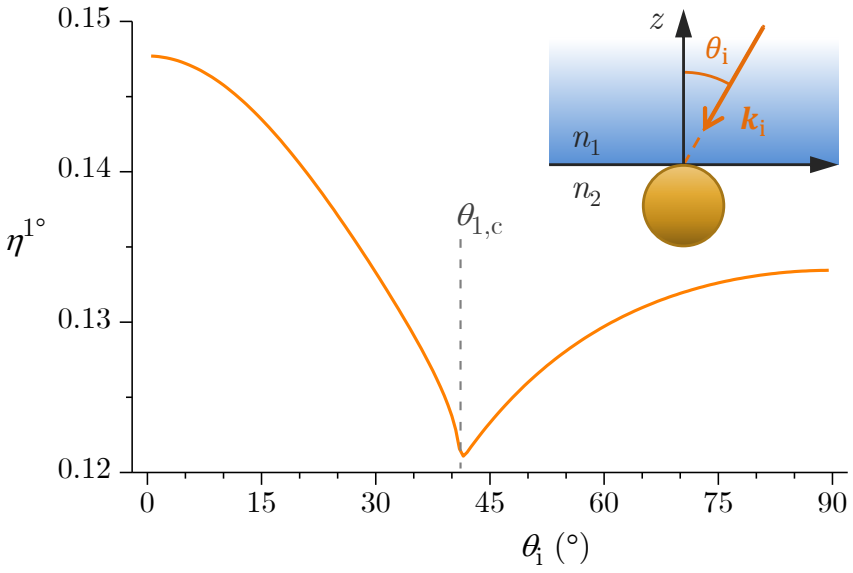

Figure S5. Fraction η^{1° of scattering collected by the objective (NA = 0.95) for a polar range of incidence $\theta_i \pm 0.5^\circ$. The scatterer is a small sphere in air ($n_2 = 1.00$) placed onto a glass substrate ($n_1 = 1.52$), see sketch. The critical angle $\theta_{1,c} = 41.1^\circ$ is indicated.

- For $\theta_i \geq \theta_{1,c}$ one has $\Theta_p = 0$; having both p and s dipoles a fixed orientation, the trend is ruled by their relative amplitudes. Specifically, $|t_p|$ decreases more rapidly than $|t_s|$, and therefore the relative contribution to P_{obj} of the s dipole — which is favorably oriented with respect Ω_{obj} — increases with θ_i.

Polarization in the total internal reflection regime A peculiar property of the evanescent wave is the elliptical polarization of its p component. Indeed, in the plane of incidence, choosing $\varphi_i = 0$ for simplicity, $\widehat{\boldsymbol{E}}_{t,p}$ according to Eq. (S6p) is written as

$$\widehat{\boldsymbol{E}}_{t,p} = \widehat{\boldsymbol{\theta}}(\theta_t) = \begin{bmatrix} \cos\theta_t \\ 0 \\ -\sin\theta_t \end{bmatrix} = \begin{bmatrix} i\sqrt{\epsilon^{-2}-1} \\ 0 \\ -\epsilon^{-1} \end{bmatrix} \quad \text{with} \quad \epsilon^{-1} = \frac{n_1}{n_2}\sin\theta_i\,. \tag{S58}$$

Therefore, $\widehat{\boldsymbol{E}}_{t,p}$ describes an ellipse of eccentricity $\sqrt{1-(\widehat{\boldsymbol{p}}_t)_x^2/(\widehat{\boldsymbol{p}}_t)_z^2} = \epsilon$ having its major axis along $\hat{\boldsymbol{z}}$. In general $1 \geq \epsilon \geq n_2/n_1$ for $\theta_{1,c} \leq \theta_i \leq \pi/2$. At $\theta_i = \theta_c$ the ellipse degenerates into a line ($\epsilon = 1$) perpendicular to the interface, while ϵ decreases for larger values of θ_i up to grazing incidence, where the polarization is almost circular ($\epsilon \ll 1$) for highly mismatched interfaces ($n_1 \gg n_2$).

In Eq. (S57) we have set $\boldsymbol{p}_p \parallel \hat{\boldsymbol{z}}$ in the TIR regime, thereby neglecting the elliptic polarization of the exciting evanescent wave. This approximation cannot be easily avoided since the analytical expressions of $\mathcal{P}(\theta,\varphi)$ presented in Sec. S.V A specifically refer to a dipole oscillating along a given direction. On the other hand, its effect on the calculated scattering parameters is expected to be only a few %; let us present here a qualitative argument to estimate the error in η^l. The largest error occurs for a quasi-circular polarization state, which is generated at near-grazing incidence for a highly-mismatched interface, and can be decomposed into an x and a z component of almost equal magnitude. If any effect of coherence between the two components is neglected, they excite two incoherent dipoles.

Our approximation then consists in replacing the x dipole with a second z one. The effect of rotating by 90° a dipole out of two can be assessed in Fig. S5, by comparing $\theta_\mathrm{i} = 0$ where $\boldsymbol{p}_\mathrm{p}$, $\boldsymbol{p}_\mathrm{s} \perp \widehat{\boldsymbol{z}}$, and a certain θ_i value in the TIR range where $\boldsymbol{p}_\mathrm{p} \parallel \widehat{\boldsymbol{z}}$ instead in our approximation. For a glass/air interface this value must be $\theta_\mathrm{i} = 51°$, where $|t_\mathrm{p}| = |t_\mathrm{s}|$ and thus $p_\mathrm{p} = p_\mathrm{s}$ (as also is for $\theta_\mathrm{i} = 0$). The collected fraction of p-excited scattering is therefore underestimated by $\eta^l\big|_{\theta_\mathrm{i}=0} - \eta^l\big|_{\theta_\mathrm{i}=51°} = 0.022$ as can be observed in Fig. S5; that is, 17 % of $\eta^l\big|_{\theta_\mathrm{i}=51°}$.

Now, η^l results from a p contribution underestimated by the amount calculated above, and an s contribution which is not affected by our approximation. The s polarization contributes approximately twice as much because $|t_\mathrm{s}| = 1.5\,|t_\mathrm{p}|$ at near-grazing incidence and due to the more favorable orientation of the s dipole with respect to the collection. Therefore the overall underestimate of η^l is slightly above 5 %. Furthermore, we emphasize that this argument refers to a worse-case scenario, whereas a significantly smaller error is expected in typical experimental conditions where

1. near-grazing incidence angles are hardly accessed ($\overline{\theta}_\mathrm{i}^\mathrm{DF} = 59°$ is the maximum value used in our high-NA measurements);
2. the glass/water and glass/air interfaces commonly used are only moderately mismatched, resulting in rather large values of ϵ.

Homogeneous environment For $n = 1$ and $(\underline{\theta}_\mathrm{d}, \overline{\theta}_\mathrm{d}) = (0, \pi)$ both terms of the integrand in Eq. (S57) reduce to $P_\mathrm{tot}/P_\mathrm{iso} = 1$ and the equation reduces to

$$P^l_\mathrm{sca} \propto 2\int_{\underline{\theta}^l_\mathrm{i}}^{\overline{\theta}^l_\mathrm{i}} \sin\theta_\mathrm{i}\,\mathrm{d}\theta_\mathrm{i} = -\cos\theta_\mathrm{i}\Big|_{\underline{\theta}^l_\mathrm{i}}^{\overline{\theta}^l_\mathrm{i}}. \tag{S59}$$

For $n = 1$ and $(\underline{\theta}_\mathrm{d}, \overline{\theta}_\mathrm{d}) = (\theta_\mathrm{obj}, \pi)$ Eq. (S57) becomes instead

$$P^l_\mathrm{obj} \propto \int_{\underline{\theta}^l_\mathrm{i}}^{\overline{\theta}^l_\mathrm{i}} \mathrm{d}\theta_\mathrm{i}\ \sin\theta_\mathrm{i} \int_0^{\alpha_\mathrm{obj}} \mathrm{d}\theta_2\ \sin\theta_2\ \frac{3}{8}\Big\{3 + 3\cos^2\theta_\mathrm{i}\cos^2\theta_2 - \cos^2\theta_\mathrm{i} - \cos^2\theta_2\Big\}. \tag{S60}$$

Eq. (S59) and Eq. (S60) are respectively the denominator and the numerator of η^l; after some algebraic simplifications we find

$$\eta^l \equiv \frac{P_\mathrm{obj}}{P_\mathrm{sca}} = \frac{1}{8}\Big[\Big(8{-}9\cos\alpha_\mathrm{obj}{+}\cos^3\alpha_\mathrm{obj}\Big){+}\Big(\cos^2\overline{\theta}_\mathrm{i}{+}\cos\overline{\theta}_\mathrm{i}\cos\underline{\theta}_\mathrm{i}{+}\cos^2\underline{\theta}_\mathrm{i}\Big)\Big(\cos\alpha_\mathrm{obj}{-}\cos^3\alpha_\mathrm{obj}\Big)\Big]. \tag{S61}$$

In the limit of small NAs, $\overline{\theta}_\mathrm{i}, \underline{\theta}_\mathrm{i} \ll 1$, Eq. (S61) simplifies to the expression (S49) found for $(\alpha_{xx}, \alpha_{yy}, \alpha_{zz}) = (\alpha, 0, 0)$, as expected.

S.VI. CHARACTERIZATION OF THE EXPERIMENTAL ILLUMINATION

The analytical calculations presented in the previous sections assumed that the condenser lens is a perfect aplanat with a homogeneous illumination in the BFP. In this section we discuss how to realize these conditions using a commercial microscope, the extent to which they are verified in our experimental set-up, and how to correct for eventual deviations.

We produced a homogeneous intensity over the BFP by inserting an engineered diffuser (Thorlabs, ED1-C20) in the illumination path before the field diaphragm. According to the manufacturer's specifications, the angular distribution of the transmitted intensity displays a *top-hat* pattern, namely approximately flat for $|\theta| < 11°$ and steeply dropping off to zero outside this central range.

We measured the illumination power in the BFP, P_{BFP}, by scanning a photodiode (Thorlabs, power meter PM100 + Si sensor S120B) along a diameter of the circular region corresponding to the condenser maximum aperture. To increase the spatial resolution, the sensor was covered by a dark mask with a circular opening of 2 mm diameter, corresponding to 0.07 NA. The results are reported in Fig. S6a for scans along and across the orientation of the image of the bulb filament, which is visible without the diffuser. The power is rather flat over most of the NA range of the condenser, and displays a drop larger than 10 % only for $\mathrm{NA_i} > 1.2$. The profile across the filament is less flat, suggesting that the filament image is not completely

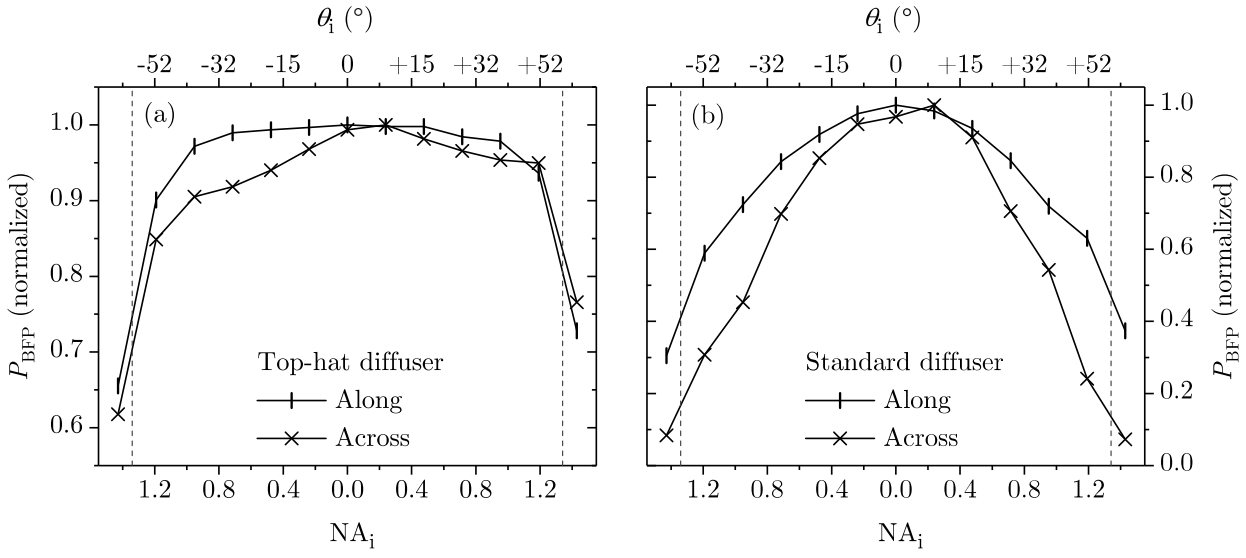

Figure S6. Illumination power in the BFP P_{BFP} as a function of the numerical aperture of illumination $\mathrm{NA_i}$ for (a) a top-hat diffuser and (b) a standard diffuser and 4:3 beam expander. The power was measured along a straight line through the center, under the same condition as the experiments presented in the paper. The directions along and across refer to the orientation of the image of the bulb filament. The vertical lines at $\mathrm{NA_i} = 1.34$ indicate the maximum NA of the condenser aperture.

erased by the diffuser. This brings about a slight dependence on φ_i of the illumination on the sample plane, which we have neglected in our analytical description. To obtain an even flatter illumination in the BFP of the condenser, one can introduce a 4:3 beam expander (Nikon MEL59500 T-C High NA Common Condenser Lens Unit) in front of the condenser, at the expense of the total illumination power. In comparison, the standard diffuser from Nikon along with the 4:3 expander provides the profile shown in Fig. S6b, where P_BFP reduces to half of the peak power at $\mathrm{NA_i} \simeq 1.2$, and to less than one third at $\mathrm{NA_i} \simeq 1.34$.

The NA dependence of the power P_i impinging on the sample is additionally affected by the dependence of the transmission of the condenser on $\mathrm{NA_i}$, which is expected to be lower at high NA due to stronger reflections from the internal optical interfaces at higher angles of incidence. We therefore we measured directly $P_\mathrm{i}(\mathrm{NA_i})$ after the condenser. To do so, we pierced a circular aperture of 1.8 mm diameter in a dark mask placed in the BFP of the condenser, so that the illumination is a light needle of well defined $\mathrm{NA_i}$. The mask was mounted on a slider to allow a continuous variation of $\mathrm{NA_i}$ along the direction of the bulb filament. Absolute NA reading was provided by a ruler (white stripe of paper in the top left corner of Fig. S7, left) calibrated with an interpolation of the known NAs of four different microscope objectives and the condenser itself. A half-ball lens attached to the front lens of the condenser as shown in Fig. S7 (left) transmits the light needle with the same efficiency for all $\mathrm{NA_i}$ values, mimicking the $n = 1.52$ immersion medium. The transmitted P_i is measured with a photodiode (Thorlabs, power meter PM100 + Si sensor S120B). The data shown in Fig. S7 (right) refer to the spectral band $\lambda = (600 \pm 20)$ nm; no relevant differences were observed across the whole investigated spectral range 400 nm to 750 nm. The overall trend resembles the one in Fig. S6, but the reduction of P_i towards large NAs is somewhat stronger. For instance, at $\mathrm{NA_i} = 1.20 \pm 0.05$, P_i is reduced by 25 % with respect to the peak value, whereas in the BFP only about 10 % are seen. Note however the error bars, indicating that each data point incorporates some contributions from larger values of $\mathrm{NA_i}$ too.

In order to minimize systematics when adopting our quantitative method, one should avoid the largest NA range for illumination — $\mathrm{NA_i} > 1.2$ for our set-up according to Fig. S7 (right). Furthermore, the angular dependence of the illumination can be characterized experimentally as just described, and taken into account in the analysis as we will now discuss. The main effect of a reduction of P_i at large NAs is to reduce the DF illumination with respect to the intensity that would be produced by the idealized system. As a result $\xi \equiv I_\mathrm{i}^\mathrm{BF}/I_\mathrm{i}^\mathrm{DF}$ is underestimated and so is $\sigma_\mathrm{sca}^\mathrm{DF}$, which is proportional to ξ. Now, I_i^l appearing in the definition of ξ is the intensity of the illumination traversing the sample plane, which the experimental cross-section are referenced to. In these supporting information we have called the same quantity I_FFP^l, and derived its expression in Eq. (S18)–(S20). We can introduce the angular dependence of P_i in the integral to calculate a generalized ξ factor, namely

$$\tilde{\xi} = \frac{\int_{A_\mathrm{i}^\mathrm{BF}} P_\mathrm{i}(\theta_\mathrm{i})\,\mathrm{d}A_\mathrm{BFP}}{\int_{A_\mathrm{i}^\mathrm{DF}} P_\mathrm{i}(\theta_\mathrm{i})\,\mathrm{d}A_\mathrm{BFP}} = \frac{\int_{\underline{\theta}_\mathrm{i}^\mathrm{BF}}^{\theta_\mathrm{i}^\mathrm{BF}} P_\mathrm{i}(\theta_\mathrm{i}) \cos\theta_\mathrm{i} \sin\theta_\mathrm{i}\,\mathrm{d}\theta_\mathrm{i}}{\int_{\underline{\theta}_\mathrm{i}^\mathrm{DF}}^{\theta_\mathrm{i}^\mathrm{DF}} P_\mathrm{i}(\theta_\mathrm{i}) \cos\theta_\mathrm{i} \sin\theta_\mathrm{i}\,\mathrm{d}\theta_\mathrm{i}}. \tag{S62}$$

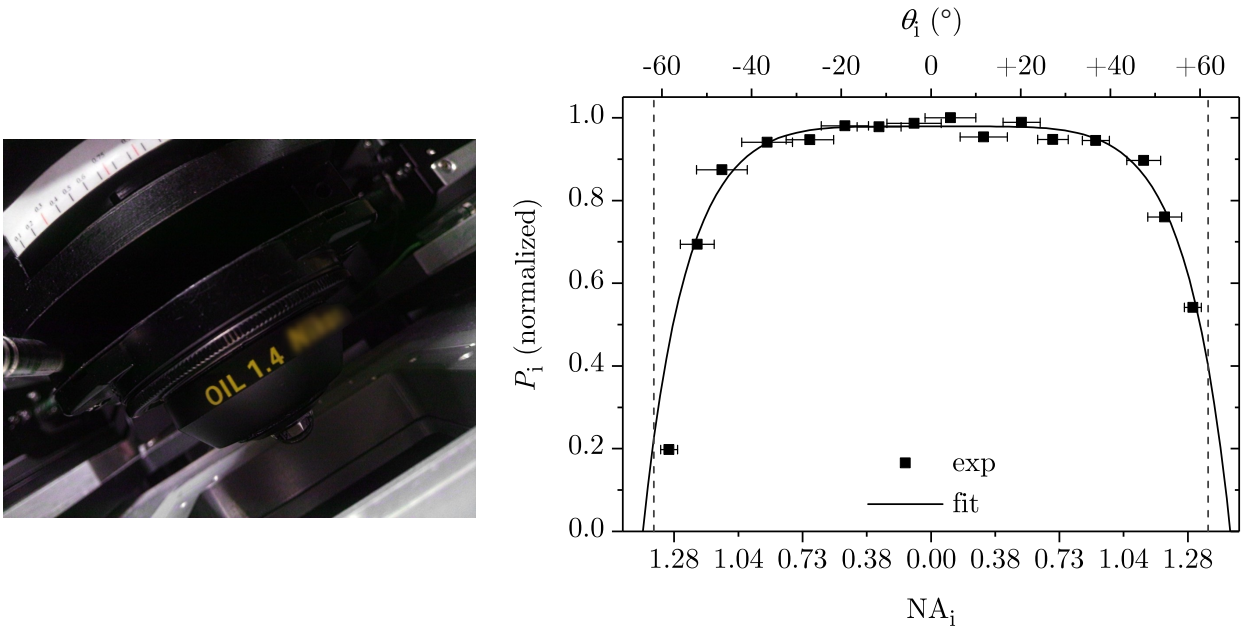

Figure S7. (Left) The condenser with a half-ball lens attached to the front lens. The lens is held in place by the surface tension of a thin layer of immersion oil. Note that although the lens casing reads 1.4, the maximum aperture of the condenser is 1.34 NA. The manufacturer logo on the barrel has been digitally blurred. (Right) Normalized illumination power P_i transmitted by the condenser as a function of the numerical aperture of illumination $\mathrm{NA_i}$, measured under the same condition as the experiments presented in the paper. $\mathrm{NA_i}$ is varied in the direction along the bulb filament image in the BFP of the condenser. The solid line is the fit to the data given by Eq. (S63). The vertical lines at $\mathrm{NA_i} = 1.34$ indicate the maximum NA of the condenser aperture.

It is easy to see that $\tilde{\xi}$ reduces to Eq. (3) of the paper for $P_\mathrm{i}(\theta_\mathrm{i}) = 1$. To compute the integrals in Eq. (S62) one can use an analytic form of $P_\mathrm{i}(\theta_\mathrm{i})$. We used the function

$$P_\mathrm{i}(\theta_\mathrm{i}) = P_\mathrm{i}(0) - \left(\frac{\theta_\mathrm{i}}{\tilde{\theta}_\mathrm{i}}\right)^a - \left(\frac{\theta_\mathrm{i}}{\tilde{\theta}_\mathrm{i}}\right)^b \quad \text{with} \quad P_\mathrm{i}(\theta_\mathrm{i}) = 0.98,\, a = 5,\, b = 10,\, \tilde{\theta}_\mathrm{i} = 1.26\,\mathrm{rad} \qquad \text{(S63)}$$

which provides a good fit to the experimental data as shown in Fig. S7. For the illumination ranges $\mathrm{NA_i^{BF}} \in [0, 0.95]$ and $\mathrm{NA_i^{DF}} \in [1.1, 1.3]$ —which we used for the polystyrene bead experiment —Eq. (S62) and (S63) yield $\tilde{\xi} = 2.54$. With respect to the uncorrected value $\xi = 1.88$, this brings about a 35 % increase in $\sigma_\mathrm{sca}^\mathrm{DF}$, which is included in the quantitative measurements in Fig. 5 of the paper. This effect is suppressed when the largest illumination NAs are not included: For instance reducing the DF range to $\mathrm{NA_i^{DF}} \in [1.1, 1.2]$ —which we used for the gold rod experiment —the correction amounts only to 17 %.

Another consequence of a reduced DF illumination is the underestimate of $\zeta \equiv P_\mathrm{sca}^\mathrm{BF}/P_\mathrm{sca}^\mathrm{DF}$ calculated for the idealized illumination. A larger ζ results in a smaller $\sigma_\mathrm{sca}^\mathrm{BF}$ according to Eq. (7a) of the paper; however, this scattering correction is negligible for absorption-

dominated NanOs, such as the metal nanoparticles we investigated in this work. We have not included any corrections to ξ and ζ in the analysis of the gold spheres and rods in order to retain the simplicity of the analytical approach, and considering that the discrepancy with simulations is governed by other, larger systematics. We will show in future works how to increase the accuracy of our quantitative method with various improvements both in the experiment and in the analysis procedure, including corrections as discussed above.

S.VII. ADDITION OF DAMPING TO THE PERMITTIVITY

The lifetime of the localized surface plasmon resonances (LSPRs) sustained by metal NanOs is limited by both radiative and non-radiative processes, corresponding respectively to scattering and absorption of light. Non-radiative relaxation mechanisms can be further distinguished: Let us call *intrinsic* those mechanisms present in a defect-free infinite crystal, i.e. collisions of electrons with other electrons and the ionic lattice; all other channels, such as collisions of electrons with lattice defects and the specimen surface, are lumped together into the denomination of *extrinsic*. In numerical modeling, radiative damping is automatically accounted for by the electromagnetic solver, whereas non-radiative damping is included via the material properties, specifically via $\operatorname{Im}\varepsilon$.

In this work $\varepsilon(\omega)$ of gold was taken from the experimental data sets by Johnson and Christy [S9], McPeak *et al.* [S10], and Olmon *et al.* [S11]. These were measured via spectroscopic ellipsometry on thin films deposited in vacuum, barring the last one, which characterized (among other samples) a single crystalline optically-thick layer. The measured $\varepsilon(\omega)$ are therefore expected to include some amount of extrinsic damping, due to sample imperfections (especially for Ref. [S9]) and surface contributions (which affect reflection measurements). Nonetheless, the simulated spectra consistently exhibit sharper LSPRs than our experiments, indicating the NanOs we measured have a larger extrinsic damping. We ascribe this to surface contributions (collisions of electrons with the surface become frequent for a particle of size comparable to the electron mean free path, which is about 40 nm in gold), to chemical interface damping (due to molecules chemically adsorbed onto the NanO surface, see Ref. [S12]) and, for the gold spheres only, to crystalline defects observed in transmission electron microscopy (TEM), see Fig. 3a of the paper. Additionally, also the radiative damping resulting from numerical simulations is inaccurate to some extent, since it refers to NanOs of idealized shape and homogeneous material.

In order to reproduce the experimental cross-section spectra, and hence perform a more reliable optical sizing, the material properties used in numerical models must represent as accurately as possible the measured NanOs. We therefore modified the permittivity as in a previous work by our group [S13]. First, the aforementioned experimental data sets were fitted with an analytical expression $\varepsilon(\omega)$ in the spectral range of interest (350 nm to 900 nm). Second, the expression thereby found was modified to include the additional

damping exhibited by each individual NanO. To carry out the first step, we split the material response into the contributions of free and bound electrons ($\varepsilon = \varepsilon_\mathrm{f} + \varepsilon_\mathrm{b}$) and provide the analytical expression of the two terms.

Free electrons The Drude model describes the free electron response as

$$\varepsilon_\mathrm{f} = \varepsilon_\infty - \frac{\gamma_0 \sigma_0}{\omega(\omega + i\gamma_0)} = \varepsilon_\infty + i\sigma_0 \left(\frac{1}{\omega} - \frac{1}{\omega + i\gamma_0} \right) \quad \text{with} \quad \sigma_0 = \frac{\omega_\mathrm{p}^2}{\gamma_0} \tag{S64}$$

where γ_0 is the angular rate of electron relaxation, σ_0 is the real DC conductivity, ω_p is the plasma frequency, and ε_∞ is the high frequency limit of $\varepsilon(\omega)$. The low energy part of the permittivity —say for $\lambda > 700\,\mathrm{nm}$— is fitted well by Eq. (S64) for the data sets by Johnson and Christy and McPeak *et al.*, as will be shown below. On the other hand, a satisfactory agreement could not be reached with the data set by Olmon *et al.*.

Now, in the standard Drude model, the frequency dependence of the damping and the charge carrier mass are neglected. In the last equality of Eq. (S64) ε_f is decomposed into two poles; to include such dependencies, following Ref. [S14], we can split the pole at $\omega = -i\gamma_0$ into two (or possibly more) distinct poles of the same form

$$\varepsilon_\mathrm{f} = \varepsilon_\infty + i\sigma_0 \left(\frac{1}{\omega} - \frac{1-\beta}{\omega + i\gamma_1} + \frac{\beta}{\omega + i\gamma_2} \right) \quad \text{with} \quad \sigma_0 = \frac{\omega_\mathrm{p}^2}{(1-\beta)\,\gamma_1 + \beta\gamma_2}. \tag{S65}$$

Note that this expression preserves causality as well as the asymptotic behavior of Eq. (S64) (ω^{-1} at low frequencies and ω^{-2} at high frequencies), and reduces to the original expression for $\beta = 0$ or $\beta = 1$. A good fit to the data set by Olmon *et al.* was obtained by adding a small contribution $\beta \sim 10^{-4}$ of a pole corresponding to a much higher scattering rate, see the fitting parameters reported in Table S1 (top).

Bound electrons The analytical model developed by Rosei [S15] and Guerrisi *et al.* [S16] describes the response of bound electrons in gold. Following Eq. (9) of Ref. [S16], the absorption is the sum of the contributions of the main optical transitions t active in the spectral range of interest

$$\mathrm{Im}\,\varepsilon_\mathrm{b} = \frac{2}{3} \left(\frac{2\pi\hbar^2 e}{m_e \omega} \right)^2 \sum_t A_t J_t(\omega) \quad \text{with} \quad t = X,\, L_{5+6}^+,\, L_4^+. \tag{S66}$$

Specifically, X indicates the interband transition from the d band to the Fermi surface near the X point of the Brillouin zone, while L_4^+ and L_{5+6}^+ indicate the transitions near the L point from the $4d$ and $5d$+$6d$ bands, respectively. The transition strengths A_t in Eq. (S66) are related to the square of the corresponding dipole transition matrix elements P_t via

$$A_X = \frac{P_X}{2\sqrt{2}\,\pi^2\hbar^3} \sqrt{\frac{m_{p\parallel}^X}{m_\mathrm{e}^2} \frac{m_{p\parallel}^X m_{p\perp}^X m_{d\parallel}^X m_{d\perp}^X}{m_{p\parallel}^X m_{d\perp}^X + m_{p\perp}^X m_{d\parallel}^X}} \tag{S67-X}$$

$$A_{L_i^+} = \frac{P_{L_i^+}}{2\sqrt{2}\,\pi^2\hbar^3} \sqrt{\frac{m_{p\parallel}^L}{m_\mathrm{e}^2} \frac{m_{p\parallel}^L m_{p\perp}^L m_{d\parallel}^{L_i^+} m_{d\perp}^{L_i^+}}{m_{p\parallel}^L m_{d\perp}^{L_i^+} + m_{p\perp}^L m_{d\parallel}^{L_i^+}}} \tag{S67-L}$$

Table S1. Parameters for fitting the analytical model of $\varepsilon(\omega)$ described in this section to various experimental data set. Top table: Parameters affecting the free electron part of ε; Bottom table: Parameters affecting the bound electron part of ε.

Experimental data set	ε_∞	$\hbar\omega_\mathrm{p}$ (eV)	$\hbar\gamma_1$ (meV)	$\hbar\gamma_2$ (eV)	β (10^{-4})
Johnson and Christy	1.9	8.78	63.8	–	0
McPeak *et al.*	2.1	9.23	39.5	–	0
Olmon *et al.*	2.0	8.65	36.2	3.29	3.9

Experimental data set	$\hbar\omega_7^X$ (eV)	$\hbar\omega_6^X$ (eV)	$\hbar\omega_{5+6}^{L^+}$ (eV)	$\hbar\omega_4^{L^+}$ (eV)	$\hbar\omega_4^{L^-}$ (eV)	P_X ($\frac{1}{e^2\mathrm{m}^3}$)	$P_{L_{5+6}^+}$ ($\frac{1}{e^2\mathrm{m}^3}$)	$P_{L_4^+}$ ($\frac{1}{e^2\mathrm{m}^3}$)	b
Johnson and Christy	0.9	1.47	1.42	2.60	0.72	1.28	5.64	3.60	2.5
McPeak *et al.*	1.1	1.48	1.45	2.44	0.72	0.80	7.49	3.20	3.0
Olmon *et al.*	1.0	1.48	1.49	2.44	0.72	0.96	6.20	2.20	4.0

where $i = 4$ or $5+6$. We fixed the values of the effective electron masses to the ones reported in Ref. [S13], and used P_X, $P_{L_{5+6}^+}$, and $P_{L_4^+}$ as fitting parameters. The joint density J_t of each transition appearing in Eq. (S66) can be expressed as

$$J_t(\omega) = \int_{\underline{\omega}_t}^{\overline{\omega}_t} \frac{f_d(\omega') - f_p(\omega, \omega')}{k_t(\omega, \omega')} \hbar \, \mathrm{d}\omega' \,, \tag{S68}$$

where the occupation probabilities of the p and d bands are given by the Fermi–Dirac distributions

$$f_p = \left(1 + \exp \frac{\hbar\omega'}{k_\mathrm{B}T}\right)^{-1} \tag{S69p}$$

$$f_d = \left(1 + \exp \frac{\hbar\omega' - \hbar\omega}{k_\mathrm{B}T}\right)^{-1} \tag{S69d}$$

using the electron temperature $T = 300\,\mathrm{K}$ and defining the origin of the energy scale at the Fermi level. The functions k_t are modeling the inverse density of states close to the respective

points in the Brillouin zone,

$$k_X = \sqrt{\hbar}\sqrt{\omega - \omega' - \omega_7^X + \frac{m_{p\parallel}^X}{m_{d\parallel}^X}\left(\omega' - \omega_6^X\right)} \tag{S70-X}$$

$$k_{L_i^+} = \sqrt{\hbar}\sqrt{\omega - \omega' - \omega_4^{L^-} - \omega_i^{L^+} + \frac{m_{p\perp}^L}{m_{d\perp}^{L_i^+}}\left(\omega' + \omega_4^{L^-}\right)} \tag{S70-L}$$

and the transition energies $\hbar\omega_7^X$, $\hbar\omega_6^X$, $\hbar\omega_{5+6}^{L^+}$, $\hbar\omega_4^{L^+}$, and $\hbar\omega_4^{L^-}$ are left as free fitting parameters. The integration limits in Eq. (S68) near the X point are $\underline{\omega}_X = -20k_\mathrm{B}T/\hbar$ and

$$\overline{\omega}_X = \begin{cases} \omega_6^X + (\omega - \omega_7^X - \omega_6^X)\frac{m_{d\parallel}^X}{m_{p\parallel}^X - m_{d\parallel}^X} & \text{for } \omega \leq \omega_7^X + \omega_6^X \\ \omega_6^X + (\omega - \omega_7^X - \omega_6^X)\frac{m_{d\perp}^X}{m_{p\perp}^X + m_{d\perp}^X} & \text{for } \omega > \omega_7^X + \omega_6^X \end{cases}. \tag{S71}$$

Near the L point the minimum of the integration interval is

$$\underline{\omega}_{L_i^+} = -\omega_4^{L^-} - \frac{\pi^2 e\hbar^2}{32a^2}\frac{1}{m_{p\parallel}^L} + \frac{m_{p\perp}^L}{m_{p\perp}^L + m_{d\perp}^{L_i^+}}\left[\omega - \omega_i^{L^+} + \frac{\pi^2 e\hbar^2}{32a^2}\left(\frac{1}{m_{p\parallel}^L} + \frac{1}{m_{d\parallel}^{L_i^+}}\right)\right] \tag{S72}$$

where the lattice parameter of gold is $a = 4.08\,\text{Å}$. Note that some typos have been corrected with respect to the corresponding Eq. (A22) in Ref. [S13]. The maximum of the integration interval is

$$\overline{\omega}_{L_i^+} = \begin{cases} -\omega_4^{L^-} + (\omega - \omega_i^{L^+})\frac{m_{d\parallel}^{L_i^+}}{m_{d\parallel}^{L_i^+} - m_{p\parallel}^L} & \text{for } \omega \leq \omega_i^{L^+} \\ -\omega_4^{L^-} + (\omega - \omega_i^{L^+})\frac{m_{d\perp}^{L_i^+}}{m_{d\perp}^{L_i^+} + m_{p\perp}^L} & \text{for } \omega > \omega_i^{L^+} \end{cases}. \tag{S73}$$

In order to reproduce in the model the broadening of the transition energies, we convolute $\mathrm{Im}\,\varepsilon_\mathrm{b}$ obtained via (S66) with a Lorentzian function

$$B(\omega) = \frac{\hbar b\gamma_0}{2\pi\hbar^2\left(\omega^2 - b^2\gamma_0^2/4\right)}, \tag{S74}$$

where b is an fitting parameter scaling the broadening relative to the Drude broadening. For fitting the data set by McPeak *et al.*, this broadening was modeled with the function

$$B(\omega) = \frac{1.76}{2\hbar b\gamma_0}\cosh^{-2}\left(\frac{1.76\omega}{b\gamma_0}\right) \tag{S75}$$

having the same full width at half maximum (FWHM) as the Lorentzian, but exponential tails which are a better approximation of the physical lineshape when the scattering energies of the interacting bath are limited, creating a non-Markovian dephasing with finite memory

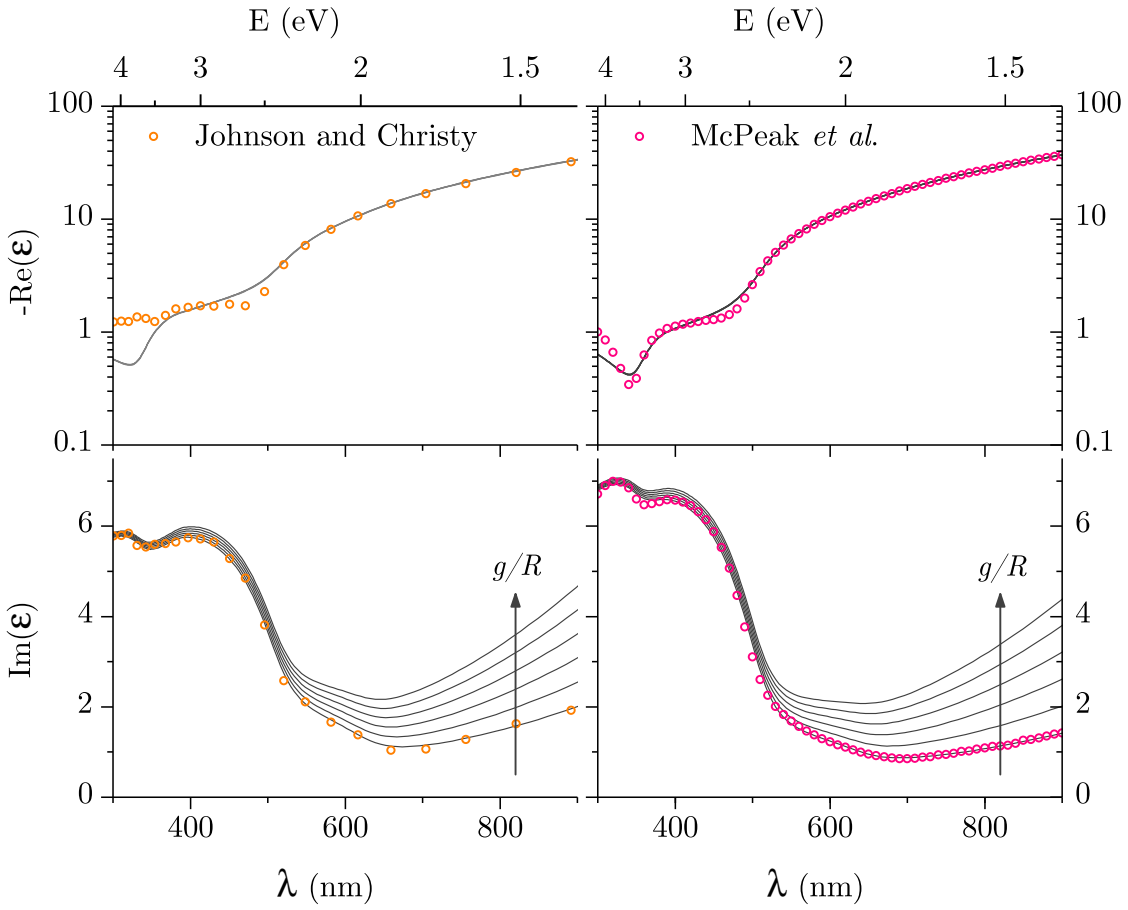

Figure S8. Symbols: Relative permittivity ε of a thin gold film measured by Johnson and Christy (left) and McPeak *et al.* (right). Lines: Fit with the analytical model described in this section; a variable damping was added as per Eq. (S76) with $g/R = 0$ to $100\,\mu\mathrm{m}^{-1}$ in steps of $20\,\mu\mathrm{m}^{-1}$.

time. When the modified Drude model (S64) including an additional pole is used, γ_0 in Eq. (S74) and Eq. (S75) is substituted with $(1-\beta)\gamma_1 + \beta\gamma_2$.

After determining $\mathrm{Im}\,\varepsilon_\mathrm{b}$ with this model, $\mathrm{Re}\,\varepsilon_\mathrm{b}$ is determined via the Kramers–Krönig transform using the causality of the material response.

The analytical model just outlined with the parameters reported in Table S1 provides a good fit to all the considered data sets. This is shown in Fig. S8 for the data set by Johnson and Christy and McPeak *et al.*, which we have used in this work for the optical sizing of the gold spheres and the gold rods, respectively. The two experimental permittivities feature a few noteworthy differences. $\mathrm{Re}\,\varepsilon_\mathrm{b}$ for McPeak *et al.* displays a clearer signature of the interband transitions below 400 nm and follows more closely the theoretical spectrum. It exhibits as well a stronger free electron contribution, $\mathrm{Re}\,\varepsilon_\mathrm{f}$ being about 10 % larger in absolute terms than Johnson and Christy, which entails a blue shift of the LSPR by about 5 nm for the gold spheres and 20 nm for the gold rods, see Fig. 3d and Fig. 4e of the paper. Lastly,

$\mathrm{Im}\,\varepsilon$ by McPeak *et al.* is lower for wavelengths longer than 500 nm, resulting to sharper LSPRs, as will be shown in the following. All these observations point towards a better crystalline quality of the film measured by McPeak *et al.*, and indeed their work focuses mainly on optimizing deposition procedures.

As discussed at the beginning of this section, metal NanOs often exhibit experimentally a larger damping than numerical simulations using bulk data sets. To better reproduce experiments, one can modify the analytical $\varepsilon(\omega)$ found by fitting. Specifically, we have increased the damping of the free electrons (to account for their additional collisions with the NanO surface and crystal defects) by replacing γ_0 in Eq. (S64) with

$$\gamma = \gamma_0 + \frac{g}{R} v_\mathrm{F} \tag{S76}$$

where $v_\mathrm{F} = 1.4 \times 10^6\,\mathrm{m/s}$ is the Fermi velocity and g an adimensional factor which parametrizes the magnitude of the extrinsic damping of the NanO. When the modified Drude model (S65) is used, both γ_1 and γ_2 are increased in this manner. It is customary in literature to factor out a R^{-1} size dependence in Eq. (S76), because surface scattering is assumed to be dominant extrinsic damping mechanism in small NanOs, and for small spheres it is expected to scale as R^{-1}, both in a classical billiard-type picture and in the quantum box model proposed first by Kawabata and Kubo [S17]. In the spectral range of interest Eq. (S64) reduces to

$$\varepsilon_\mathrm{f} = \varepsilon_\infty - \frac{\omega_\mathrm{p}^2}{\omega^2+\gamma^2}\left(1 - i\frac{\gamma}{\omega}\right) \xrightarrow{\omega \gg \gamma} \varepsilon_\infty - \frac{\omega_\mathrm{p}^2}{\omega^2}\left(1 - i\frac{\gamma}{\omega}\right) \tag{S77}$$

so that $\mathrm{Re}\,\varepsilon_\mathrm{f}$ is unaffected whereas $\mathrm{Im}\,\varepsilon_\mathrm{f}$ increases linearly with g/R, as observed in Fig. S8.

We are now able to assess the effect of the additional damping on our numerical simulations. In Fig. S9 the full width at half maximum (FWHM) of the main dipolar LSPR is plotted for the gold spheres and rods (longitudinal mode) investigated in this work as a function of g/R. For a fixed particle geometry (average deduced from electron microscopy), the FWHM increases linearly with the damping to a good approximation, except for Olmon *et al.*, where the modified Drude model (S65) was used. The simulated FWHM can be compared to the experimental linewidth represented by the horizontal dashed lines, so that the intersection of these lines with the fit of the simulated data point individuates graphically the estimated value of g/R for each particle.

For spheres (Fig. S9a) we compared the three data sets considered in this work. The linewidth at $g = 0$ reflects the bulk damping γ_0 of each data set, and is smaller for McPeak *et al.* because of its smaller $\mathrm{Im}\,\varepsilon$ at λ_LSPR. Consequently, a larger value of g is required to reproduce the experimental linewidth when McPeak *et al.* is used. Values of g around unity are in line with previous experimental reports in literature [S13, S18, S19].

For rods (Fig. S9b), we considered only the data set by McPeak *et al.*, which provides the best agreement with the experimental spectroscopy, see Fig. 4e of the paper. On the other hand, different environments are compared, with the interesting finding that g/R is systematically larger in air than in oil for the same rod. In fact, a dependence on the

particle surroundings cannot be explained appealing to surface damping alone, and suggests that other mechanisms such as chemical interface damping play as well a role in gold rods, as recently reported by other groups, see Ref. [S12]. Notably, the average g/R in oil is significantly smaller for rods than for spheres: $30\,\mu\mathrm{m}^{-1}$ versus $140\,\mu\mathrm{m}^{-1}$ (it seems more meaningful to refer to g/R rather than g when comparing different particle shapes). When correlated to the TEM images reported in the paper, which display a high crystalline quality of rods (Fig. 4a) but not of spheres (Fig. 3a), this suggests that — in contrast to what is typically assumed in literature — for spheres of the investigated size a major portion of the extrinsic damping is due to crystal defects rather than surface scattering. In fact, the values of g we have found are larger than the theoretical estimate $g_{\mathrm{s}} = 0.73$ for surface damping alone calculated via the quantum-box model in Ref. [S17].

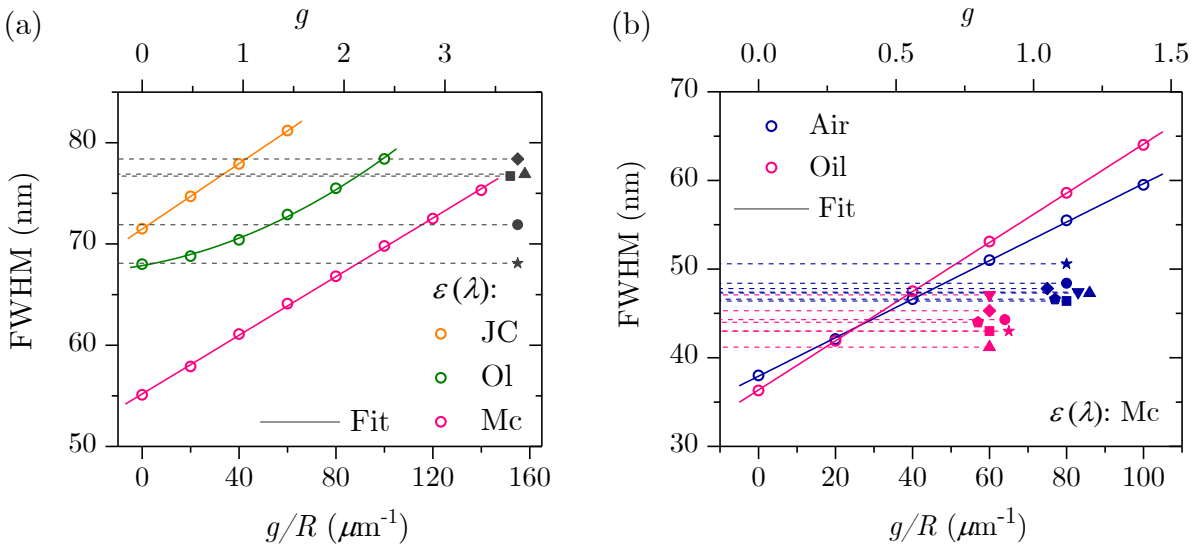

Figure S9. Hollow circles: Simulated FWHM of the main dipolar LSPR as a function of the extrinsic damping factor g. Bulk $\varepsilon(\lambda)$ experimental data sets by Johnson and Christy (JC), Olmon *et al.* (Ol), and McPeak *et al.* (Mc). Lines: Linear (JC, Mc) or parabolic (Ol) fits. Horizontal dashed lines: FWHM of the experimental single-particle spectra. Each particle is identified by a symbol at the end of the line (at an arbitrary horizontal position), which correlates to Fig. 3d–e of the paper for the spheres and to Fig. 4e–f for the rods. (a) Sphere of radius $R = 29\,\mathrm{nm}$ (average from TEM characterization) in a $n = 1.52$ environment. (b) Rod of width $W = 28\,\mathrm{nm}$ (average from TEM characterization) and aspect ratio $AR = 2.43$ in air ($n = 1.00$) and $AR = 2.45$ in oil ($n = 1.52$) (AR adjusted to have the longitudinal LSPR at the average experimental $\lambda_{\mathrm{LSPR}} = 605\,\mathrm{nm}$ in air, and $\lambda_{\mathrm{LSPR}} = 695\,\mathrm{nm}$ in oil), placed on a $n = 1.52$ glass substrate.

S.VIII. OPEN DATA

The following materials are available free of charge in the open data repository of Cardiff University at the DOI: 10.17035/d.2018.0064868399.

1. The raw data of all the figures presented in the paper and the supporting information.
2. Structural characterization of the investigated colloids, including a larger set of electron microscopy images than what shown in the paper for the metallic particles.
3. The COMSOL models we used to simulate the scattering and the absorption of the investigated NanOs, along with an extensive data set of gold permittivity modified with additional damping.
4. A MATLAB code to compute the scattering parameters implementing the analytical model presented above.
5. Experimental characterization of the microscope illumination, to back up the assumptions of the analytical description of it we have put forward.
6. The raw detected spectra and the quantitative cross-section spectra for all the 5 spheres and 7 rods we have measured; these worksheets (produced by the Origin software) can be used as templates for the quantitative analysis.

Generally speaking, we provide as open data all the materials that can help other users to implement our analysis technique using their own microscope. The data set includes an HTML index page which describes in detail the materials therein contained, and points to the specific data corresponding to each figure panel.

[S1] L. Payne, W. Langbein, and P. Borri, Extinction suite plug-in for ImageJ.

[S2] L. Payne, W. Langbein, and P. Borri, Polarization-resolved extinction and scattering cross-sections of individual gold nanoparticles measured by wide-field microscopy on a large ensemble, Appl. Phys. Lett. **102**, 131107 (2013).

[S3] L. Payne, G. Zoriniants, F. Masia, K. P. Arkill, P. Verkade, D. Rowles, W. Langbein, and P. Borri, Optical micro-spectroscopy of single metallic nanoparticles: Quantitative extinction and transient resonant four-wave mixing, Faraday Discuss. **184**, 305 (2015).

[S4] L. Payne, A. Zilli, Y. Wang, W. Langbein, and P. Borri, Quantitative high-throughput optical sizing of individual colloidal nanoparticles by wide-field imaging extinction microscopy, in *Proc. SPIE 10892, Colloidal Nanoparticles for Biomedical Applications XIV*, 108920J (2019).

[S5] W. Lukosz and R. Kunz, Fluorescence lifetime of magnetic and electric dipoles near a dielectric interface, Opt. Commun. **20**, 195 (1977).

[S6] W. Lukosz and R. E. Kunz, Light emission by magnetic and electric dipoles close to a plane interface. I. Total radiated power, J. Opt. Soc. Am. **67**, 1607 (1977).

[S7] W. Lukosz and R. E. Kunz, Light emission by magnetic and electric dipoles close to a plane dielectric interface. II. Radiation patterns of perpendicular oriented dipoles, J. Opt. Soc. Am. **67**, 1615 (1977).

[S8] W. Lukosz, Light emission by magnetic and electric dipoles close to a plane dielectric interface. III. Radiation patterns of dipoles with arbitrary orientation, J. Opt. Soc. Am. **69**, 1495 (1979).

[S9] P. B. Johnson and R. W. Christy, Optical constants of noble metals, Phys. Rev. B **6**, 4370 (1972).

[S10] K. M. McPeak, S. V. Jayanti, S. J. P. Kress, S. Meyer, S. Iotti, A. Rossinelli, and D. J. Norris, Plasmonic films can easily be better: Rules and recipes, ACS Photon. **2**, 326 (2015).

[S11] R. L. Olmon, B. Slovick, T. W. Johnson, D. Shelton, S.-H. Oh, G. D. Boreman, and M. B. Raschke, Optical dielectric function of gold, Phys. Rev. B **86**, 235147 (2012).

[S12] B. Foerster, A. Joplin, K. Kaefer, S. Celiksoy, S. Link, and C. Sönnichsen, Chemical interface damping depends on electrons reaching the surface, ACS Nano **11**, 2886 (2017).

[S13] F. Masia, W. Langbein, and P. Borri, Measurement of the dynamics of plasmons inside individual gold nanoparticles using a femtosecond phase-resolved microscope, Phys. Rev. B **85**, 235403 (2012).

[S14] J. W. Allen and J. C. Mikkelsen, Optical properties of CrSb, MnSb, NiSb, and NiAs, Phys. Rev. B **15**, 2952 (1977).

[S15] R. Rosei, Temperature modulation of the optical transitions involving the Fermi surface in Ag: Theory, Phys. Rev. B **10**, 474 (1974).

[S16] M. Guerrisi, R. Rosei, and P. Winsemius, Splitting of the interband absorption edge in Au, Phys. Rev. B **12**, 557 (1975).

[S17] A. Kawabata and R. Kubo, Electronic properties of fine metallic particles. II. Plasma resonance absorption, J. Phys. Soc. Jpn. **21**, 1765 (1966).

[S18] S. Berciaud, L. Cognet, P. Tamarat, and B. Lounis, Observation of intrinsic size effects in the optical response of individual gold nanoparticles, Nano Lett. **5**, 515 (2005).

[S19] O. L. Muskens, P. Billaud, M. Broyer, N. Del Fatti, and F. Vallée, Optical extinction spectrum of a single metal nanoparticle: Quantitative characterization of a particle and of its local environment, Phys. Rev. B **78**, 205410 (2008).